

# Positron Emission Tomography

The second major method for tomographic imaging in nuclear medicine is *positron emission tomography* (PET). This mode can be used only with positron-emitting radionuclides (see Chapter 3, Section G). PET detectors detect the “back-to-back” annihilation photons that are produced when a positron interacts with an ordinary electron. Although the annihilation photons could be detected using single photon emission computed tomography (SPECT) systems operating in conventional single-photon counting mode, these systems are not optimally designed for the relatively high energy of annihilation photons (511 keV). They have relatively low detection efficiencies at these energies and require relatively inefficient high-energy collimators. As well, SPECT systems do not take advantage of the back-to-back directional characteristics of annihilation photons. This unique feature is exploited advantageously with special annihilation-coincidence detector systems for PET.

PET has gained widespread clinical acceptance and now is firmly established alongside planar imaging and SPECT in clinical nuclear medicine. In this chapter, we describe the basic features of annihilation coincidence detection, the design and performance characteristics of PET detectors and scanners, and some of the important clinical applications of PET.

## A. BASIC PRINCIPLES OF PET IMAGING

### 1. Annihilation Coincidence Detection

When a positron undergoes mutual annihilation with a negative electron, their rest masses are converted into a pair of annihilation photons (see Fig. 3-7). The photons have identical energies (511 keV) and are emitted

simultaneously, in 180-degree opposing directions, usually within a few tenths of a mm to a few mm of the location where the positron was emitted, depending on the energy and range of the positrons. Near-simultaneous detection of the two annihilation photons allows PET to localize their origin along a line between the two detectors, without the use of absorptive collimators. This mechanism is called *annihilation coincidence detection* (ACD). Detection of a pair of annihilation photons in opposing detectors actually defines the volume from which they were emitted. Most ACD detectors have square or rectangular cross sections. Thus the volume is essentially a box of square or rectangular cross section, with dimensions equal to those of the detectors (Fig. 18-1).

Coincidence logic (Chapter 8, Section F and Fig. 8-15) is employed to analyze the signals from the opposing detectors. For many PET scanners, this is accomplished by having the electronics attach a digital “time stamp” to the record for each detected event. Typically, this is done with a precision of approximately 1 or 2 nanoseconds ( $1 \text{ nsec} = 10^{-9} \text{ sec}$ ). The coincidence processor examines the time stamp for each event in comparison with events recorded in the opposing detectors. A coincidence event is assumed to have occurred when a pair of events are recorded within a specified *coincidence timing window*, which typically is 6 to 12 nanoseconds.

Although annihilation photons are emitted simultaneously, a small but finite coincidence window width is needed to allow for differences in signal transit times through the cables and electronics, as well as different distances of travel by the two photons from the annihilation event to the detectors (see Section A.2). In addition, the detectors in a PET scanner do not have perfect timing precision and therefore have a finite *timing*

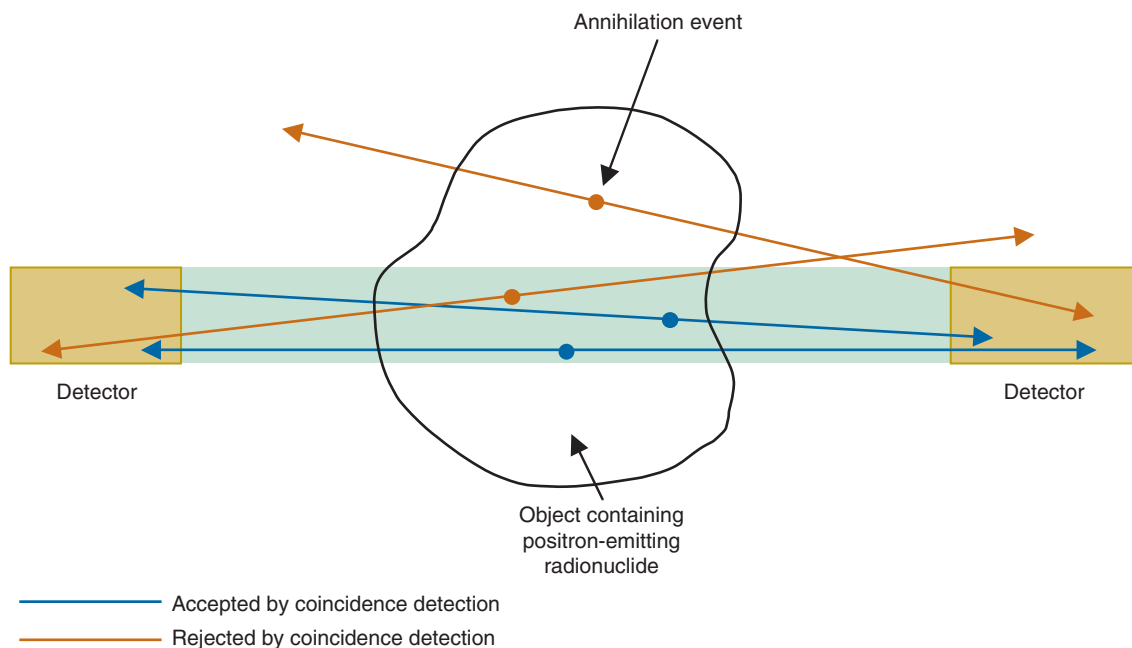


**FIGURE 18-1** Volume (green shaded area) from which a pair of simultaneously emitted annihilation photons can be detected in coincidence by a pair of detectors. Not all decays in this volume will lead to recorded events, because it is necessary that both photons strike the detectors. Outside the shaded volume, it is impossible to detect annihilation photons in coincidence unless one or both undergo a Compton scatter in the tissue and change direction.

*resolution.* Uncertainties that govern the timing resolution can arise from the statistical nature of the signal (which is produced by the conversion of 511-keV photons into light, electrons, or electron-hole pairs in the detector) and from electronic noise in the detector and associated circuits. Uncertainties also can arise from the electronic method used to determine the time at which the interaction occurred (see Chapter 8, Section F). For a pair of similar detectors, the timing uncertainties typically are well described by a gaussian distribution, and the timing resolution is defined as the full width at half maximum (FWHM) of this distribution. For scintillation detectors, the timing uncertainty is reduced, and the timing resolution improved, by using brighter and faster scintillators that produce a large number of light photons over a short time interval immediately after an interaction occurs. Timing resolution is typically in the range of 0.5 to 5 nsec, depending on which scintillator and photodetector is used.

The need for a finite window width permits other types of events to occur in coincidence, as discussed in Section A.9. Also, as discussed in Section A.4, the annihilation photons are not always emitted in precise back-to-back directions. The effects of these deviations from the ideal are discussed in the sections indicated.

The ability of ACD to localize events on the basis of coincidence timing, without the need for absorptive collimation, is referred to as *electronic collimation*. As was discussed in Chapter 14, Section C, the lead septa in standard parallel-hole collimators, which are necessary to obtain adequate spatial localization, also are responsible for the relatively low sensitivity of these collimators. Because ACD does not require a collimator to define spatial location, its sensitivity (number of events detected per unit of activity in the object) is much higher than is obtainable with the absorptive collimators used for conventional planar imaging and for SPECT. For comparable midplane resolution, the sensitivity of PET is many times higher than for SPECT.

In addition, by incorporating multiple opposing detectors in a complete ring or other geometric array around the patient, and operating each detector in the array in coincidence with multiple detectors on the other side of the array, data for multiple projection angles can be acquired simultaneously (Fig. 18-2). Indeed, with a stationary ring or geometric array that completely surrounds the patient, it is possible to acquire data for all projection angles simultaneously. This allows the performance of relatively fast dynamic studies and the reduction of artifacts caused by patient motion.

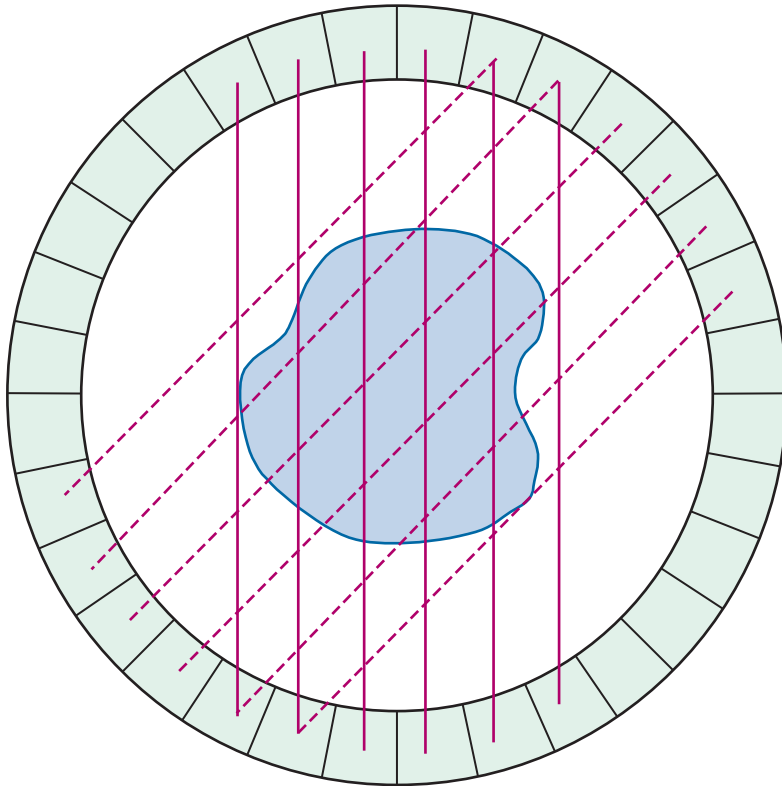


**FIGURE 18-2** Array of detectors operating in electronic coincidence with detectors on the opposite side of the ring. This allows simultaneous acquisition of projection views from many different angles. Solid and dotted lines illustrate two simultaneously acquired projection views.

## 2. Time-of-Flight PET

In theory, it is possible to determine the location along a line between the two ACD detectors at which the annihilation photons originated by determining the difference in the time at which they are detected by the two detectors. This technique, which would allow the formation of tomographic images without mathematical reconstruction algorithms, is called *time-of-flight* PET. If the difference in the arrival times of the photons is  $\Delta t$ , the location of the annihilation event, with respect to the midpoint between the two detectors, is given by

$$\Delta d = \frac{\Delta t \times c}{2} \quad (18-1)$$

where  $c$  is the velocity of light ( $3 \times 10^{10}$  cm/sec). According to this equation, to achieve 1-cm depth resolution would require timing resolution of approximately 66 picoseconds ( $1 \text{ psec} = 10^{-12} \text{ sec} = 0.001 \text{ nsec}$ ). Although electronic circuits are capable of measuring this timing difference, the rise times of light output from scintillators currently available for PET imaging are too slow to provide this

level of timing resolution. As well, the finite number of photoelectrons generated when an annihilation photon is detected gives rise to a “time jitter” during the rise time that adds to the uncertainty in event timing. This effect becomes more severe with detectors that have relatively low light output.

With the fastest available scintillators and careful design of electronic components and connections, it is possible to achieve timing accuracy at the level of a few hundred picoseconds. Although this is adequate to achieve localization only to within a few centimeters, images reconstructed from data acquired at this level of timing resolution have a higher signal-to-noise ratio than images reconstructed without time-of-flight information. This is because individual events can be constrained to lie within a smaller volume in the image reconstruction process. **Figure 18-3** illustrates how the backprojection of data along one particular line of response is constrained to a smaller region of the reconstructed image matrix by the addition of time-of-flight information. To provide practically useful levels of time-of-flight information, only the fastest and brightest scintillators,

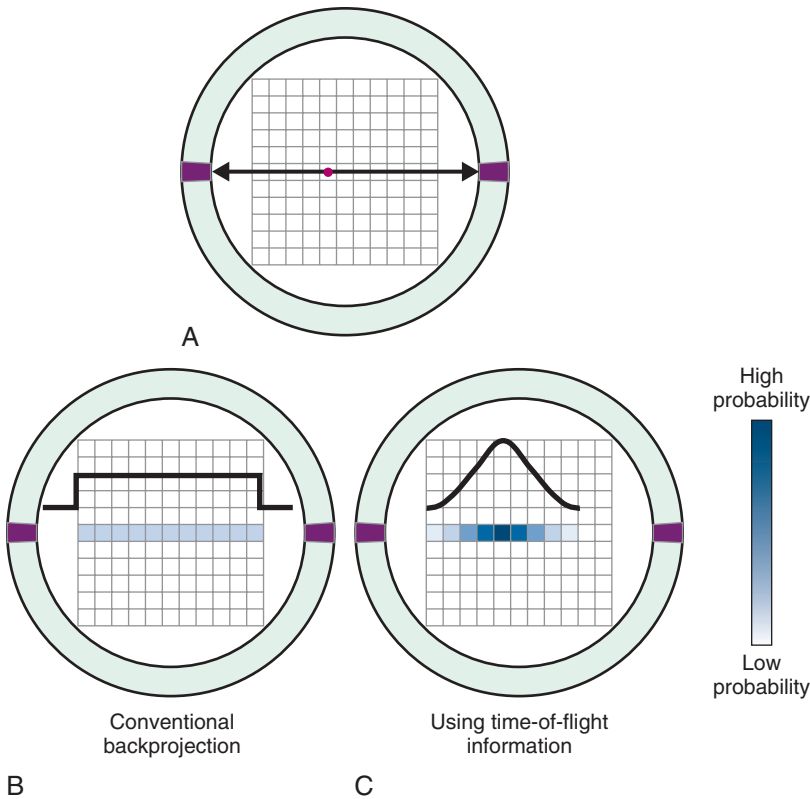


**FIGURE 18-3** A, A pair of annihilation photons are emitted from a source (red dot) and detected in coincidence by opposing detectors. B, In the absence of time-of-flight information, there is no information about the location of the source along the line joining the two detectors. During reconstruction, the event is backprojected with equal probability of having occurred in all pixels along that line. C, With time-of-flight information, some limited localization of the event is possible and events are backprojected with probabilities that follow a Gaussian distribution, centered on pixel  $\Delta d$  (Equation 18-1) from the center of the scanner and with a full width at half maximum equal to the timing resolution of the detector pair.

such as LSO and  $\text{LaBr}_3$ , can be used (see Tables 7-2 and 18-2). Several commercially built systems incorporate some level of time-of-flight information using these materials. Although there are scintillators with even faster decay components, such as  $\text{BaF}_2$ , these are not favored because the signal-to-noise improvements that can be realized from time-of-flight information is typically more than offset by their lower density and therefore lower efficiency for detecting 511-keV annihilation photons.

### 3. Spatial Resolution: Detectors

The spatial resolution of ACD with discrete detector elements is determined primarily by the size of the individual detector elements. As shown in Figure 18-4A, for elements of width  $d$ , a one-dimensional (1-D) slice through the ACD point-source response profile at midplane between the detector pair is a triangle. The detector resolution,  $R_{\text{det}}$  has a  $\text{FWHM} = d/2$ . As the source moves toward either detector, the response profile becomes trapezoidal, eventually becoming a box of width  $d$  at the face of either detector. Considering a 2-D detector with width  $d$  and height  $h$ , the ACD response profile becomes a 3-D function, which is a pyramid at midplane and

a rectangular box of area  $d \times h$  at the face of either detector. Between these extremes, it is the frustum of a pyramid with lower base size equal to the size of the detectors and upper base size increasing linearly from zero at midplane to the size of the detectors at their face.

Alternatively, consider an uncollimated pair of gamma camera detectors, also operating in coincidence mode (Fig. 18-4B). If their intrinsic spatial resolution (see Chapter 14, Section A.1) is a gaussian function with  $\text{FWHM} = R_{\text{int}}$ , then the spatial resolution of the detector pair for ACD also is a gaussian function with  $\text{FWHM} = R_{\text{int}}/\sqrt{2}$  at midplane. The ACD response profile becomes wider as the source moves toward either detector, with its FWHM eventually becoming equal to  $R_{\text{int}}$  at the face of either detector. Assuming that the resolution of the imaging detector is the same in all directions, the 2-D ACD response profile is obtained by rotating the 1-D gaussian function around its center.

For both discrete or gamma camera-type detectors, the spatial resolution of ACD varies by only approximately 30% in the central 60% of the space between the detectors (Fig. 18-5). By comparison, the resolution of a parallel-hole collimator can vary by several hundred percent over a comparable range (see Fig.

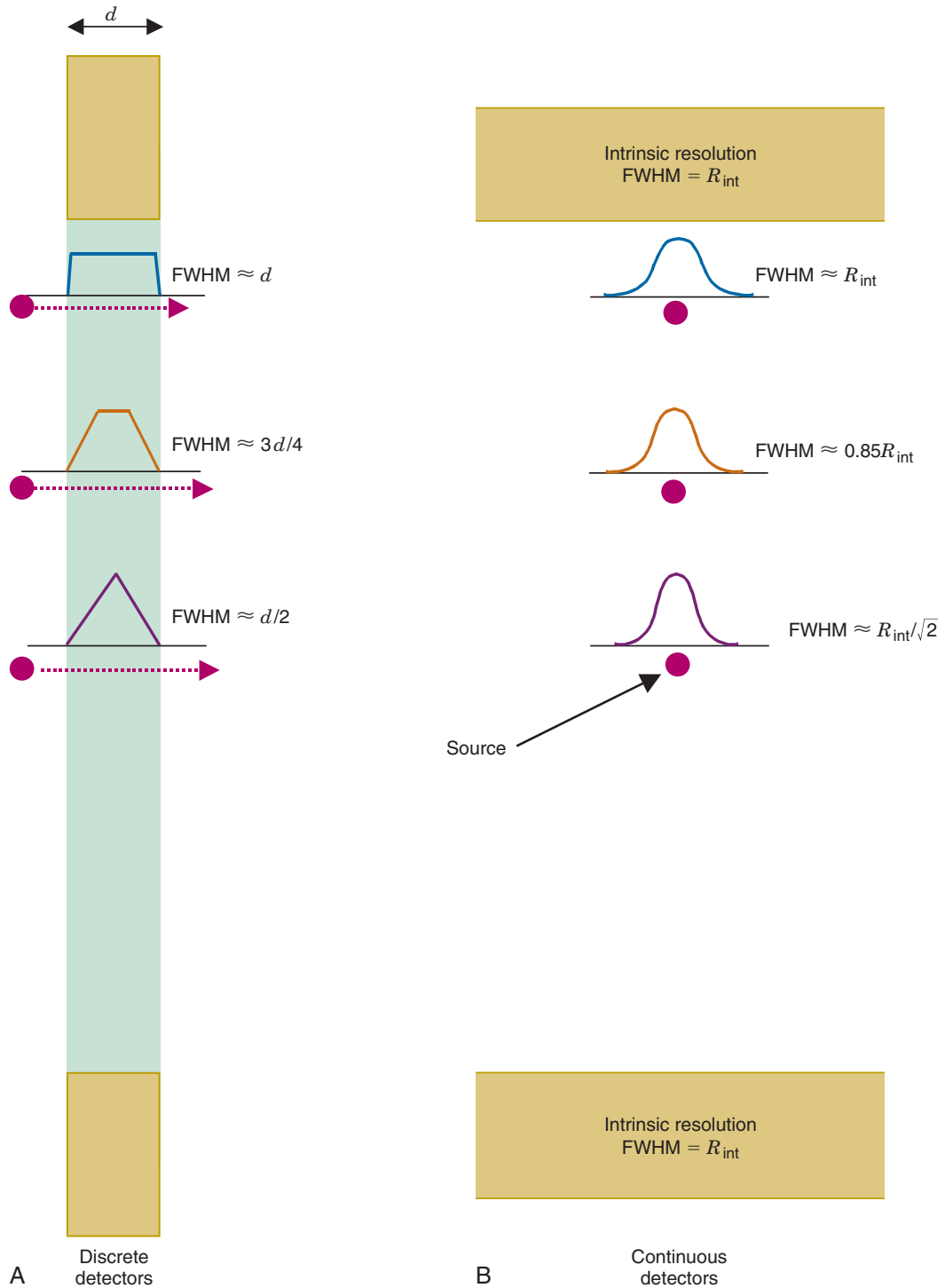


**FIGURE 18-4** Spatial resolution of detector pair ( $R_{\text{det}}$ ) for coincidence detection. **A**, For discrete detectors, spatial resolution is determined by the width of the detector element,  $d$ . At midplane, the coincidence response function is a triangle with full width at half maximum ( $\text{FWHM}$ ) =  $d/2$ . As the source is moved closer to one of the detectors, the response function becomes trapezoidal in shape, eventually becoming a rectangle of width,  $d$ . **B**, For continuous detectors, spatial resolution is determined by the intrinsic resolution of the detector,  $R_{\text{int}}$ . At the midplane, the coincidence response function is approximately gaussian, with  $\text{FWHM} = R_{\text{int}}/\sqrt{2}$ . Near the face of a detector, it becomes  $\text{FWHM} = R_{\text{int}}$ .

14-19). When profiles obtained from opposing views in SPECT are combined using the geometric mean, the variation in resolution within the space between the opposing detectors is reduced to a level comparable to ACD (see Fig. 17-8). The key difference is that the resolution of ACD is determined primarily by the size of the detector element or the intrinsic resolution of the camera detector, whereas for SPECT, the resolution is primarily determined by the collimator resolution at the *mid-point* between the two detectors. The latter is substantially degraded from its value at the face of the detector. This means that the collimator must have very high resolution at its face to achieve even moderately good resolution at midplane between the detectors. In turn, the requirement for high spatial resolution leads to relatively low detection efficiency with absorptive collimators (see Chapter 14, Section C). As discussed in Section A.8, this results in relatively low sensitivity for a SPECT system as compared with a PET system with comparable spatial resolution.

#### 4. Spatial Resolution: Positron Physics

The spatial resolution of an ACD system is degraded from the values derived from simple geometry indicated in Figure 18-4 by two factors relating to the basic physics of positron emission and annihilation. The first is the *finite range of positron travel* before it undergoes annihilation. ACD defines the line along which the annihilation event took place, which is not precisely the location from which the decaying radioactive nucleus emitted the positron. The range of travel for a positron before it undergoes annihilation is essentially the same as the range of travel of an ordinary electron (or  $\beta$  particle) of similar energy (see Chapter 6, Section B.2). Figure 6-10 and Table 6-1 show the extrapolated range versus maximum energy for  $\beta$  particles,  $E_{\beta}^{\max}$ . The maximum energies of the positrons emitted from radionuclides used for nuclear medicine are in the range of 0.5 to 5 MeV (Table 18-1; see also Appendix C). Thus their extrapolated ranges are in the 0.1- to 2-cm range.

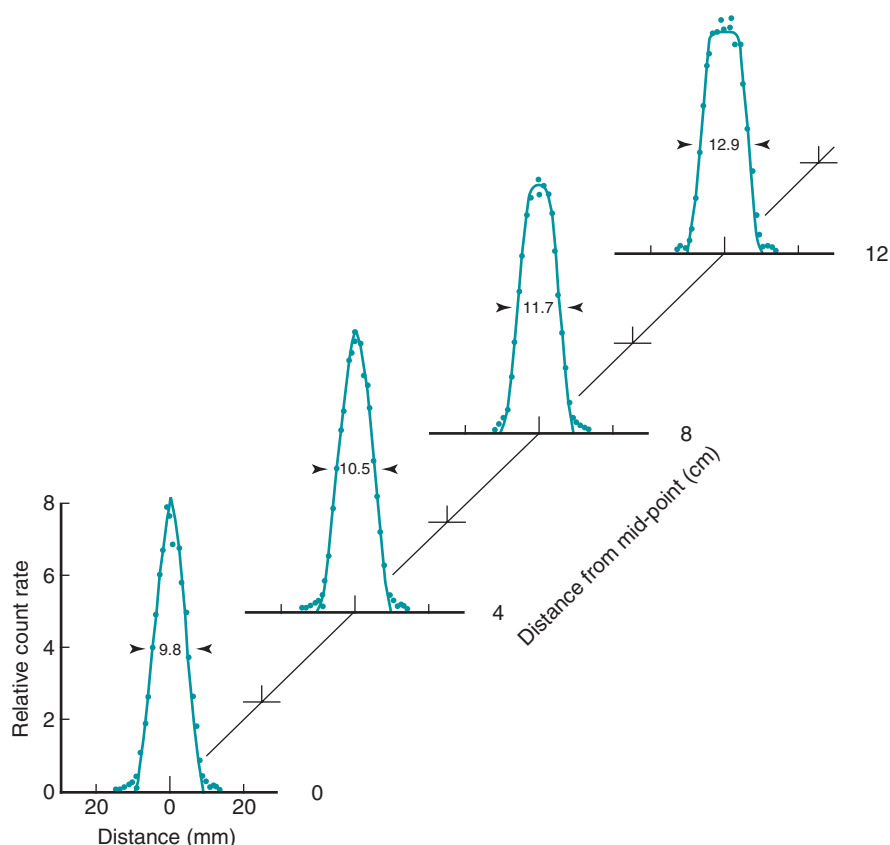


**FIGURE 18-5** Measured line-spread functions for a pair of 17-mm-wide coincidence detectors as a function of source position between the two detectors. The detector separation was 42 cm. The FWHM varies by only 30% within the central 24 cm (57%) of the space between the two detectors. (From Hoffman EJ, Huang S-C, Plummer D, Phelps ME: Quantitation in positron emission computed tomography: VI. Effect of nonuniform resolution. J Comput Assist Tomogr 6:987-999, 1982.)

**TABLE 18-1**  
**SOME POSITRON-EMITTING NUCLIDES USED FOR IN VIVO IMAGING**

Radionuclide	Half-Life	$\beta^+$ fraction	Maximum $\beta^+$ Energy	How Produced
$^{11}\text{C}$	20.4 min	0.99	960 keV	Cyclotron
$^{13}\text{N}$	9.96 min	1.00	1.19 MeV	Cyclotron
$^{15}\text{O}$	123 sec	1.00	1.72 MeV	Cyclotron
$^{18}\text{F}$	110 min	0.97	635 keV	Cyclotron
$^{62}\text{Cu}$	9.74 min	0.98	2.94 MeV	Generator (from $^{62}\text{Zn}$ )
$^{64}\text{Cu}$	12.7 hr	0.19	580 keV	Cyclotron
$^{68}\text{Ga}$	68.3 min	0.88	1.9 MeV	Generator (from $^{68}\text{Ge}$ )
$^{76}\text{Br}$	16.1 hr	0.54	3.7 MeV	Cyclotron
$^{82}\text{Rb}$	78 sec	0.95	3.35 MeV	Generator (from $^{82}\text{Sr}$ )
$^{124}\text{I}$	4.18 days	0.22	1.5 MeV	Cyclotron

The extrapolated range applies to the highest-energy positrons emitted by a radionuclide. However, positrons, like  $\beta$  particles, are emitted with a spectrum of energies. Only a small fraction have the full amount of energy available from the decay (see Fig. 3-2). In addition, the extrapolated range is the maximum distance that the electron would travel if it were not significantly deflected in any of its interactions and traveled in essentially a straight line to the end of its range. In reality, most electrons (and positrons) travel a tortuous path, often with multiple large-angle deflections (see Fig. 6-4). The

result is that the average distance measured from the origin of the positrons to the end of their path is significantly smaller than their extrapolated range.

For purposes of defining the spatial resolution of ACD, the distance of interest is the *effective positron range*. This is the average distance from the emitting nucleus to the end of the positron range, measured *perpendicular* to a line defined by the direction of the annihilation photons (Fig. 18-6). This distance always is smaller than the extrapolated range for the positrons emitted by the radionuclide.

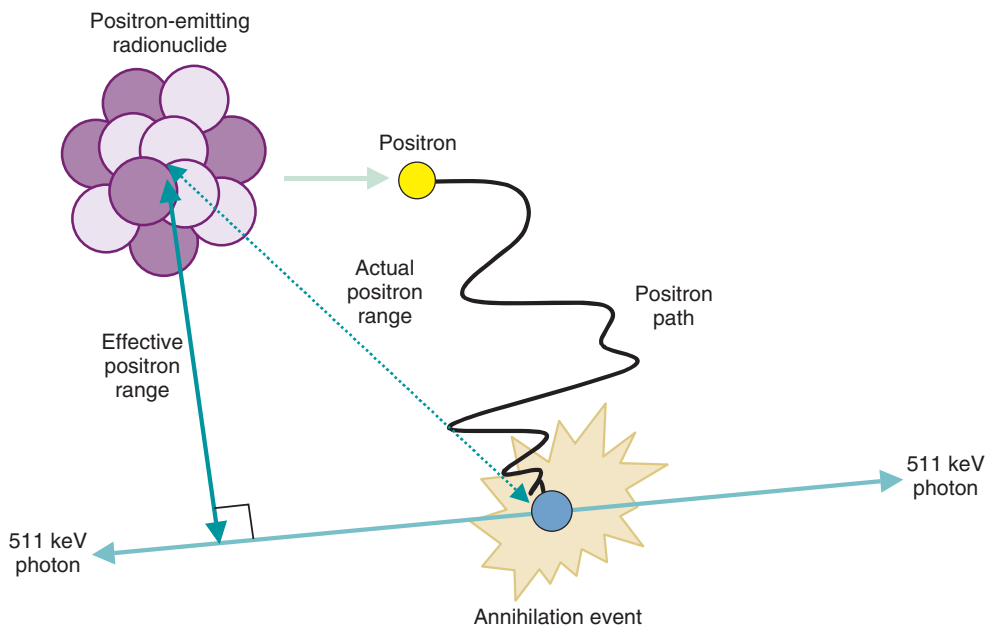


**FIGURE 18-6** Blurring caused by positron range effects. The perpendicular distance from the decaying atom to the line defined by the two 511-keV annihilation photons is referred to as the *effective positron range*.



Figure 18-7 shows the positron range distribution for point sources of  $^{18}\text{F}$  ( $E_{\beta}^{\text{max}} = 0.635 \text{ MeV}$ ) and  $^{15}\text{O}$  ( $E_{\beta}^{\text{max}} = 1.72 \text{ MeV}$ ). According to Figure 6-10, the extrapolated ranges for these positrons in water would be approximately 2 mm and 8 mm, respectively; however, the FWHMs of their distribution profiles are only 0.1 mm and 0.5 mm.

Note as well that the positron range distributions shown in Figure 18-7 have long tails and thus are not well described by gaussian functions. Therefore the FWHM is not the best indicator of the effect of positron range on ACD spatial resolution. Instead, the *root mean square (rms) effective range* often is used. Figure 18-8 shows the general relationship between rms effective range and maximum positron energy. Typical rms effective ranges (and thus the blurring caused by positron ranges) are on the order of 0.5 to 3 mm. Note that positron range is inversely proportional to the density of the absorber. Thus rms ranges would be proportionately higher in lung tissue and airways ( $\rho \sim 0.1\text{--}0.5 \text{ g/cm}^3$ ) and lower in dense tissues such as bone ( $\rho \sim 1.3\text{--}2 \text{ g/cm}^3$ ).

A second factor involving the physics of positrons is that the annihilation photons almost never are emitted at *exactly* 180-degree directions from each other (Fig. 18-9). This effect, which is due to small residual momentum of the positron when it reaches the end of its range, is known as *noncolinearity*. The angular distribution is approximately gaussian with FWHM approximately 0.5 degree. The effect on spatial resolution, expressed in terms of FWHM, is linearly dependent on the separation of the ACD detectors,  $D$ , and is given by

$$R_{180^\circ} = 0.0022 \times D \quad (18-2)$$

A typical value of  $D$  for a whole-body PET scanner is 80 cm. Thus the FWHM for blurring caused by noncolinearity is approximately 2 mm.

The *system resolution* of an ACD or PET detector system is obtained by combining the individual resolution components, in the same manner as the component resolutions are combined to determine the system resolution

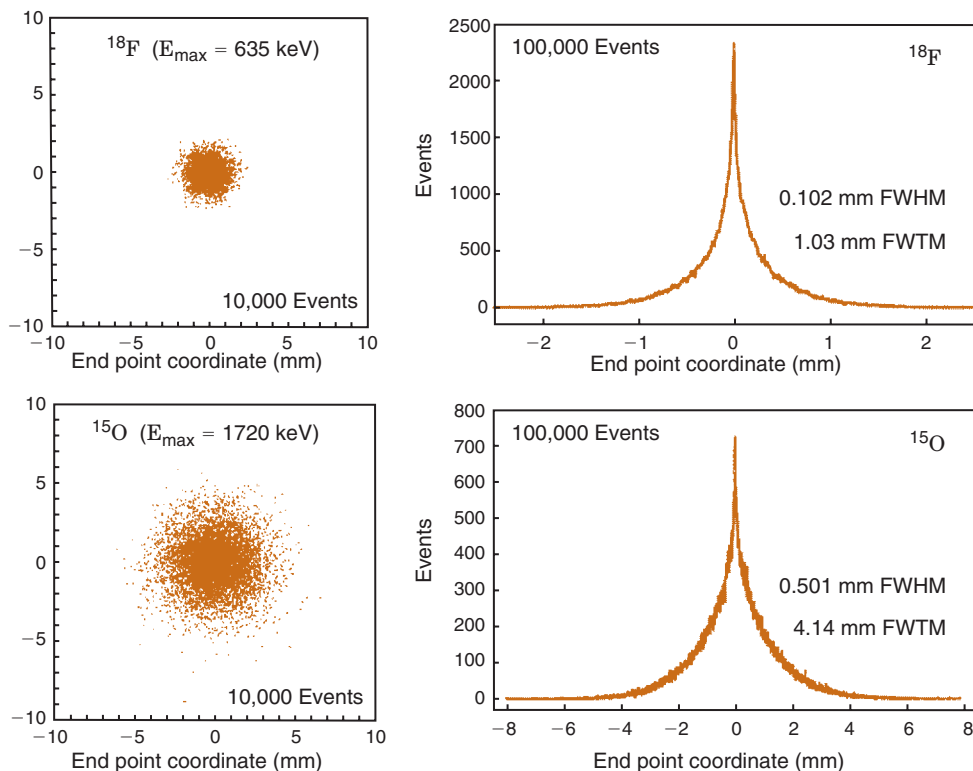


**FIGURE 18-7** Results of Monte Carlo simulations showing the distribution of annihilation sites for positron-emitting point sources in water for  $^{18}\text{F}$  ( $E_{\beta}^{\text{max}} = 0.635 \text{ MeV}$ ) and  $^{15}\text{O}$  ( $E_{\beta}^{\text{max}} = 1.72 \text{ MeV}$ ). The profile of the distribution is broader for  $^{15}\text{O}$  because of its higher average positron energy, which leads to a longer positron range prior to annihilation. (From Levin CS, Hoffman EJ: Calculation of positron range and its effect on the fundamental limit of positron emission tomography system spatial resolution. Phys Med Biol 44:781-799, 1999.)



**FIGURE 18-8** Root mean square range for positrons in water versus  $E_{\beta}^{\max}$ . (Data from Derenzo SE: *Mathematical removal of positron range blurring in high-resolution tomography*. IEEE Trans Nucl Sci 33:565-569, 1986.)

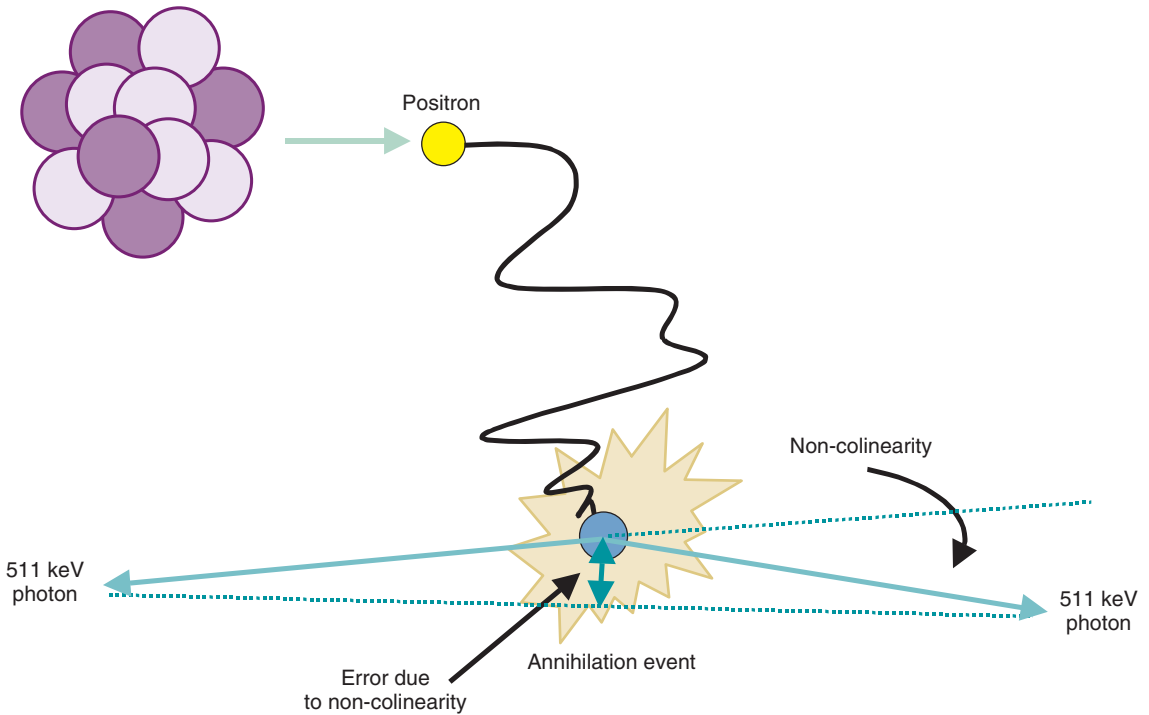
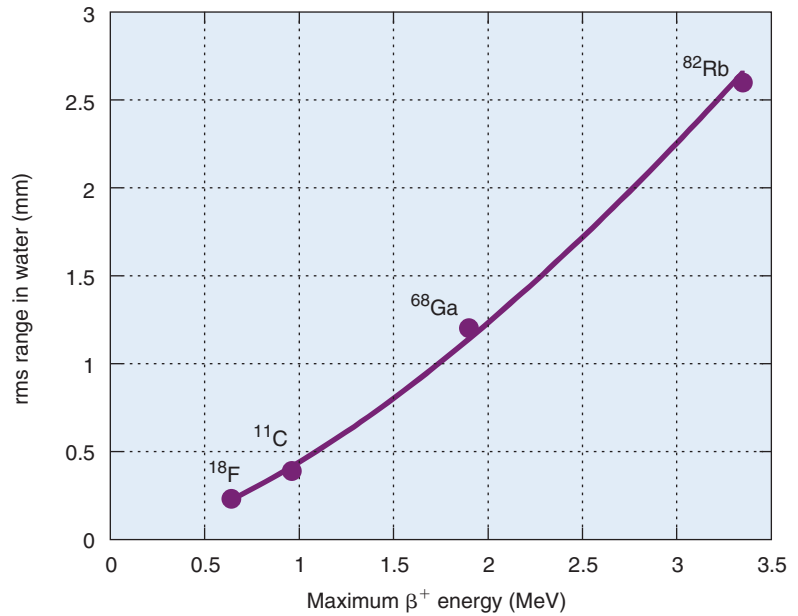


**FIGURE 18-9** Noncolinearity of annihilation photons resulting from residual momentum of the electron and positron at annihilation. Noncolinearity leads to positioning errors. Angles are exaggerated in this example for purposes of illustration. Actual range of angles is about  $\pm 0.25$  degree, centered at 180 degrees.

for a gamma camera system (see Chapter 14, Section C.4). Thus

$$R_{\text{sys}} \approx \sqrt{R_{\text{det}}^2 + R_{\text{range}}^2 + R_{180^\circ}^2} \quad (18-3)$$

where  $R_{\text{det}}$  is the spatial resolution of the detector system, as determined by the size of

the discrete detector elements or the intrinsic resolution of continuous detectors (see Section A.3 and Fig. 18-4). For typical whole-body PET scanners, with either discrete detector elements or gamma camera detectors, the effects of positron range and noncolinearity combine to add anywhere from a few tenths

of a millimeter to a few millimeters to system resolution.

### EXAMPLE 18-1

What fraction of PET system resolution at the center of the scanner bore is caused by positron range and noncolinearity blurring in the following three situations? (1) 6-mm-wide discrete detectors, separated by 80 cm, using  $^{18}\text{F}$ ; (2) 2-mm-wide discrete detectors separated by 60 cm, using  $^{68}\text{Ga}$ ; (3) gamma camera detectors with 3-mm intrinsic resolution at 511 keV, separated by 60 cm, using  $^{68}\text{Ga}$ .

Assume that the positron range distribution can be approximated by a gaussian function and use the rms effective range to represent the FWHM of that function.

#### Answer

For *situation 1*, the spatial resolution at the midpoint between 6-mm-wide discrete detectors is given by

$$R_{\text{det}} = d/2 = (6 \text{ mm})/2 = 3 \text{ mm}$$

The rms range for  $^{18}\text{F}$  is  $R_{\text{range}} \approx 0.2 \text{ mm}$  (see Fig. 18-8), and the noncolinearity for an 80-cm separation is

$$R_{180^\circ} = 0.0022 \times 800 \text{ mm} = 1.76 \text{ mm}$$

Using Equation 18-3, the system resolution is

$$R_{\text{sys}} \approx \sqrt{3^2 + 0.2^2 + 1.76^2} \approx 3.5 \text{ mm}$$

Thus resolution blurring caused by positron range and noncolinearity for situation 1 adds approximately 17% to the system resolution, relative to the detector resolution.

For *situation 2*, using the same equations and Figure 18-8, the spatial resolution of 2-mm-wide discrete detectors is  $R_{\text{det}} = 1 \text{ mm}$ , the rms range for  $^{68}\text{Ga}$  is  $R_{\text{range}} \approx 1.2 \text{ mm}$  and the noncolinearity blurring for the 60-cm separation is 1.32 mm. Thus the system resolution is

$$R_{\text{sys}} \approx \sqrt{1^2 + 1.2^2 + 1.32^2} \approx 2.05 \text{ mm}$$

In this situation, the additional blurring caused by positron range and noncolinearity approximately doubles the system resolution relative to detector resolution. Note that if  $^{68}\text{Ga}$  is replaced by the lower-energy  $^{18}\text{F}$  in

situation 2, the system resolution becomes  $\sim 1.7 \text{ mm}$ , so the effects of positron range and noncolinearity still are substantial ( $\sim 70\%$ ).

For *situation 3*,  $R_{\text{det}} = 3/\sqrt{2} \approx 2.12 \text{ mm}$  (see Fig. 18-4) while other factors remain the same as in situation 2. Thus

$$R_{\text{sys}} \approx \sqrt{3^2/2 + 1.2^2 + 1.32^2} \approx 2.77 \text{ mm}$$

Positron range and noncolinearity increase the system resolution by approximately 30% relative to detector resolution in this situation.

From Example 18-1, one can conclude that positron range and noncolinearity have a relatively small effect on system resolution for whole-body systems, which usually have larger detector elements (situation 1) or only moderately high spatial resolution (situation 3). This is especially true for  $^{18}\text{F}$ , the radionuclide most commonly used for clinical applications. However, their effects can be important limitations for high-resolution brain imaging or small-animal imaging devices (see Section B.5) that employ small discrete detector elements, especially for applications involving higher-energy positrons (situation 2).

Because they do not depend on technology, positron range and non colinearity create barriers for improving the spatial resolution of PET systems that cannot be overcome simply by using smaller detector elements. For example, independent of the detectors used, the blurring caused by noncolinearity will limit the achievable spatial resolution for a whole-body PET scanner to approximately 2 mm, because a bore size of 80-90 cm is required to accommodate the human body. Example 18-1 also demonstrates that when system resolution is dominated by one component, the gains achieved by improving other components of resolution may be small.

## 5. Spatial Resolution: Depth-of-Interaction Effect

A substantial thickness of scintillator material is required to efficiently stop 511-keV annihilation photons. In a gamma camera, typical NaI(Tl) detector crystal thicknesses are 1.25 cm or less. PET systems generally employ 2- to 3-cm-thick scintillators with greater stopping power, such as BGO or LSO. For PET systems using arrays of detectors in multiple coincidence mode around the object, the relatively thick detector elements lead to

a degradation of resolution known as the *depth of interaction* (DOI) effect. Although the effect also occurs in the axial direction in scanners that use cross-plane coincidence detection for 3-D data acquisition (see [Section C.2](#)), the primary effect is in the radial direction, and the discussion focuses on this aspect of the problem.

[Figure 18-10](#) illustrates the cause of the problem for a detector system that uses a circular array of elements, all or most elements of which operate in multicoincidence mode with other elements in the array. For a source located near the center of the scanner, spatial resolution is determined by the width of the detector element,  $R_{\text{det}} = d/2$ , as described in [Section A.3](#) and illustrated in [Figure 18-4](#). However, for a source located away from the center, the apparent width of the detector element becomes

$$d' = d \cos \theta + x \sin \theta \quad (18-4)$$

where  $d$ ,  $x$ , and  $\theta$  are as indicated in [Figure 18-10](#). The apparent change in width results from the angulation between the detectors and from lack of knowledge about the depth

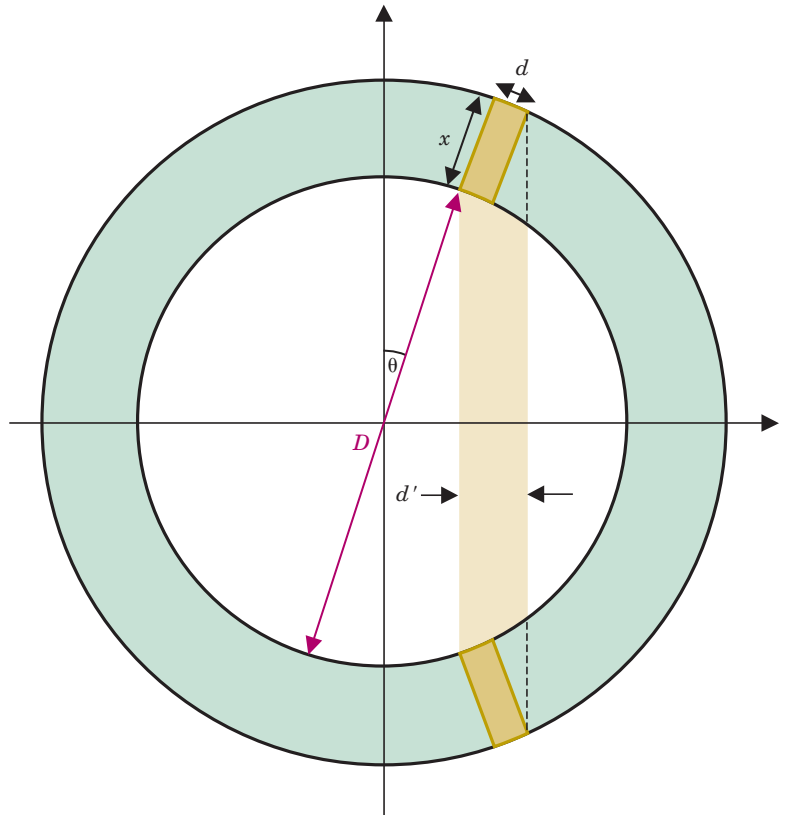
at which an interaction has occurred within the detector crystal. The spatial resolution (FWHM) then becomes  $R'_{\text{det}} = d'/2$ . Using [Equation 18-4](#), this can be written as

$$\begin{aligned} R'_{\text{det}} &\approx (d/2) \times [\cos \theta + (x/d) \sin \theta] \\ &\approx R_{\text{det}} \times [\cos \theta + (x/d) \sin \theta] \end{aligned} \quad (18-5)$$

From this equation it can be seen that the DOI effect is described by a multiplicative factor applied to the value of detector resolution at the midpoint between a pair of directly opposed detectors.

[Equation 18-5](#) is only an approximation because the thickness of detector material is not constant across the width of the detector element seen by the source. Note as well that, for thin detector elements  $[(x/d) \ll 1]$ , it is possible that  $R'_{\text{det}} < R_{\text{det}}$ . The same would be true for a very efficient detector material (or a very thin detector) that would stop most of the annihilation photons in a thin layer at the entrance to the detector. However, these conditions never apply in practice. Typically,  $x \sim 2$  to 3 cm and  $d \sim 0.3$  to 0.6 cm. For a whole-body PET scanner with 4-mm-wide detectors on a diameter of 80 cm, the DOI effect causes

**FIGURE 18-10** Apparent width of a detector element,  $d'$ , increases with increasing radial offset in a PET scanner consisting of a circular array of detector elements. Because the depths at which the  $\gamma$  rays interact within the scintillation crystal are unknown, the annihilation event for a pair of photons recorded in coincidence could have occurred anywhere within the shaded volume. The magnitude of the effect depends on the source location, the diameter of the scanner,  $D$ , the length of the crystal elements,  $x$ , and the width of the detector elements,  $d$ .



approximately a 40% degradation of resolution at a distance of 10 cm from the center of the field of view (FOV).

The DOI effect is somewhat different for systems that use hexagonal or octagonal arrays as opposed to circular arrays of detector elements. With hexagonal or octagonal arrays, as the source moves away from the center of the scanner, some portion of an opposing array still remains perpendicular to it, at least over a distance comparable to the width of a segment of the array. Consequently, there is less variation in the DOI effect across the FOV. At the center of the FOV, the effect is somewhat larger than at the center for a circular array of the same diameter, whereas at the periphery it is somewhat smaller. On average, the DOI effect is comparable for both segmented and circular arrays.

Note also in [Equations 18-4 and 18-5](#) that, for a given radial distance away from the center of the scanner,  $\theta$  and  $\sin \theta$  become smaller (and thus  $R'_{\text{det}}$  becomes smaller) as the diameter of the detector ring becomes larger. Because of the DOI effect, PET scanners often are built with detector arrays that are of larger diameter than would be necessary to fit the patient, which in turn increases detector costs.

## 6. Spatial Resolution: Sampling

In ACD, the FWHM of the detector resolution is one-half the width of a detector element (see [Fig. 18-4](#)). For a stationary array of detector elements, each of width  $d$ , the sampling interval between parallel projection lines also is  $d$  ([Fig. 18-11A](#)). Considering only detector resolution, it can be shown that this leads to undersampling of object profiles, which in turn leads to a distortion of the high-frequency content (i.e., the fine details) of the reconstructed image (see [Fig. 16-11](#) and [Section C](#)). According to [Equation 16-14](#), three samples should be acquired per FWHM of spatial resolution. In theory, this would translate into a requirement for *six* samples over an interval equal to the width of a detector element. However, as described elsewhere in this section, system resolution is degraded from the theoretical limits established by intrinsic resolution by other factors, so that coarser sampling is acceptable. Nonetheless, some additional sampling is required beyond that illustrated in [Figure 18-11A](#).

In practice, two samples usually are acquired per detector element width. Although less than the theoretical ideal, this results in little noticeable distortion of clinical images. Some

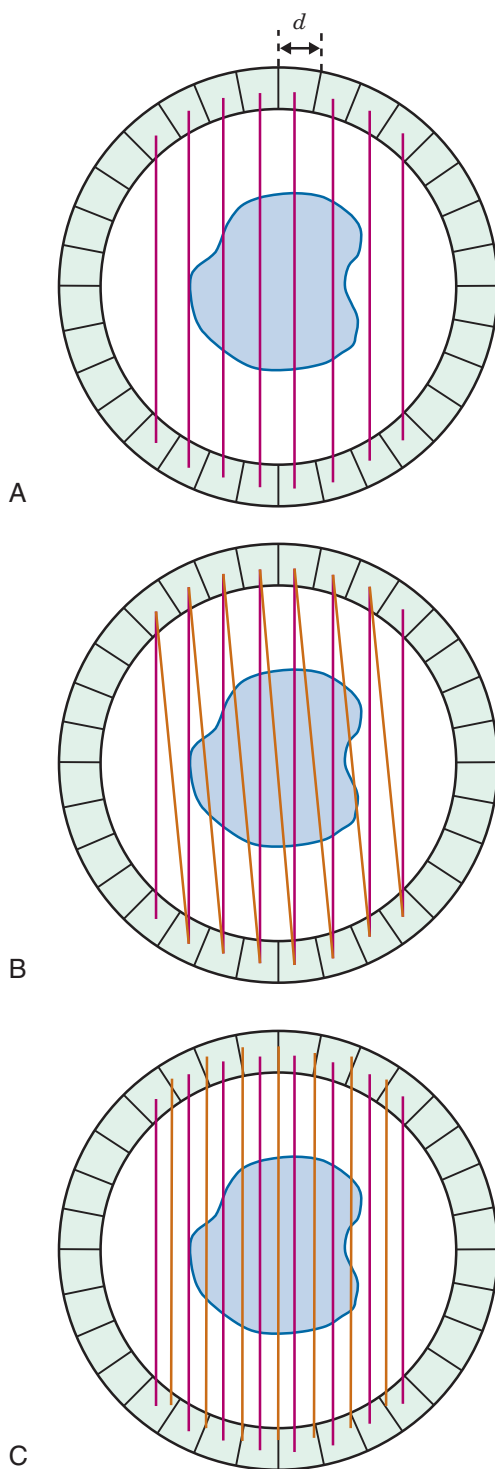


**FIGURE 18-11** A, For a stationary array of discrete detector elements, the linear sampling distance is the same as the detector element width,  $d$ , which is insufficient to support the resolution of the detectors ( $\sim d/2$ ). B, Linear sampling distance is reduced to  $d/2$  when coincidences with immediately adjacent detectors are allowed. C, For image reconstruction, these samples are treated as if they came from a set of virtual detectors offset by half the detector width relative to the actual detectors.

earlier scanners actually incorporated a mechanical shift to acquire two sets of data with the detector elements shifted by half the width of a detector element between acquisitions. This approach was mechanically cumbersome. The modern approach is to use coincidence events in adjacent pairs of detector elements, thereby creating additional samples between the detector elements, as illustrated in [Figure 18-11B](#). These are treated as samples acquired with a virtual set of detectors located between the actual detector elements, as shown in [Figure 18-11C](#). The ray paths for the additional samples are not quite parallel to those for directly opposed detectors, but this seems to have little effect on the reconstructed image across most of the useful FOV.

Note that combining data for adjacent pairs of detectors into a single projection view as illustrated in [Figure 18-11B and C](#), reduces the number of projection angles available from a stationary ring of detectors by half. Note also that PET systems that use continuous (i.e., gamma camera type) detectors (see [Section B.3](#)) can use arbitrarily chosen sampling intervals and thus can avoid some of the sampling problems associated with discrete detector arrays.

## 7. Spatial Resolution: Reconstruction Filters

The discussions in the preceding sections describe the spatial resolution achievable with PET systems, as determined by the physical characteristics of the imaging device and the basic physics of positron decay. However, as discussed in Chapter 16, Sections B.3 and C.3, spatial filters are applied to the recorded projection profiles to suppress noise in the reconstructed image (see Fig. 16-12). Inevitably, this results in some degradation of spatial resolution. In general, the fewer the number of counts recorded in an image, the lower the filter cut-off frequency ( $k_{\text{cut-off}}$ ) and the greater the loss of spatial resolution.

The selection of cut-off frequency depends in part on the type of study. Thus a brain scan might be reconstructed with a cut-off frequency yielding 6-mm spatial resolution, whereas an abdominal scan, with more tissue attenuation and generally lower count densities, might be reconstructed with a filter yielding 10-mm spatial resolution. As well, the sensitivity (number of counts recorded per unit of activity in the patient) affects the statistical quality of the image and the degree of

spatial filtering required to achieve an acceptable noise level in the image. As discussed in the following section and in [Section B](#), PET systems, especially those employing multiple detector rings and multi-ring coincidence detection, have substantially higher detection efficiencies (by orders of magnitude) than is achievable with typical SPECT systems. Thus PET images usually can be reconstructed with higher cut-off frequencies, and their final spatial resolution generally is superior to SPECT images.

## 8. Sensitivity

The sensitivity of PET, like that of all imaging devices, is determined primarily by the absorption efficiency of the detector system and its solid angle of coverage of the imaged object. The true coincidence rate,  $R_{\text{true}}$ , for a positron-emitting source located in an absorbing medium between a pair of coincidence detectors is given by

$$R_{\text{true}} = E\varepsilon^2 g_{\text{ACD}} e^{-\mu T} \quad (18-6)$$

where  $E$  is the source emission rate (positrons/sec);  $\varepsilon$  is the intrinsic efficiency of each detector, that is, the fraction of incident photons detected (Equation 11-9, assumed to be the same for both detectors); and  $\mu$  and  $T$  are the linear attenuation coefficient and total thickness of the object, respectively.  $g_{\text{ACD}}$  is the geometric efficiency of the detector pair, that is, the fraction of annihilation events in which both photons are emitted in a direction to be intercepted by the detectors.

As shown in [Figure 18-4](#), the shape as well as the amplitude of the point-source response profile (i.e.,  $g_{\text{ACD}}$  for a point source) varies with the location of the source between the two detectors. In one dimension, the profile is triangular at the midpoint between the detectors, rectangular at the face of either detector, and trapezoidal at locations between. In *two dimensions*, the ACD response at the midpoint is a pyramid, whereas at the surface of either of the detectors it is a rectangular box. At points between, it is the frustum of a pyramid. In all cases, the lower base is equal to the area of the detectors.

Maximum geometric efficiency for ACD is obtained for a point source located precisely at the midpoint of the centerline between the two detectors. However, as illustrated in [Figure 18-4](#), this value does not apply when the point source is moved even slightly away from the centerline, or from the midpoint of



that line. Thus a more appropriate measure for distributed sources is the *average* geometric efficiency within the sensitive volume for ACD. Midway between the two detectors, this is given by

$$\begin{aligned}\bar{g}_{ACD} &\approx 2 \times \frac{1}{3} \times [A_{\text{det}} / \pi D^2] \\ &\approx \frac{2A_{\text{det}}}{3\pi D^2}\end{aligned}\quad (18-7)$$

where  $D$  is the distance between the detectors and  $A_{\text{det}}$  is the area of the detector facing the source.

The term in brackets in Equation 18-7 is the geometric efficiency for a single detector for a point source located at the midpoint of the centerline between the detectors. (As discussed in Chapter 11, Section A.2, this expression is valid when the detector dimensions are “small” in comparison with the source-to-detector distance.) The factor of 2 accounts for the fact that two detectors are used and that if one photon is emitted in a proper direction toward one detector, the other photon is virtually assured of being emitted in the proper direction toward the other. The factor of  $1/3$  is the average geometric efficiency across the sensitive volume at midplane, that is, the average height of a pyramid.

Actual PET systems typically employ many small detector elements arranged in circular,

hexagonal, or octagonal arrays. Each detector element is operated in coincidence with many detectors on the opposing side of the ring, as shown in Figure 18-12. This multicoincidence operation has useful and important consequences for both the magnitude and uniformity of geometric efficiency.

The simplest way to visualize its effects on geometric efficiency is to consider a complete ring of detectors on a diameter  $D$ , with detector height  $h$  in the axial dimension and detector width  $d \ll D$  in the plane of the ring. Assume that any interdetector gaps are “very small,” so that the individual elements form a virtually continuous ring of detector material. For a point source located precisely at the center of the ring, the geometric efficiency would be equal to the solid angle subtended by the ring, because if either annihilation photon is intercepted by the ring, it is virtually assured that the second photon is traveling the proper direction to be intercepted as well. From simple geometric considerations, if  $h \ll D$ , it can be shown that the solid angle, and thus the geometric efficiency, for a point source precisely at the center of the ring is given by

$$g_{\text{ACD,RING}} \approx h/D \quad (18-8)$$

Under the conditions described, geometric efficiency is relatively constant as the source is moved away from the center of the ring but still in its center plane; however, as the source

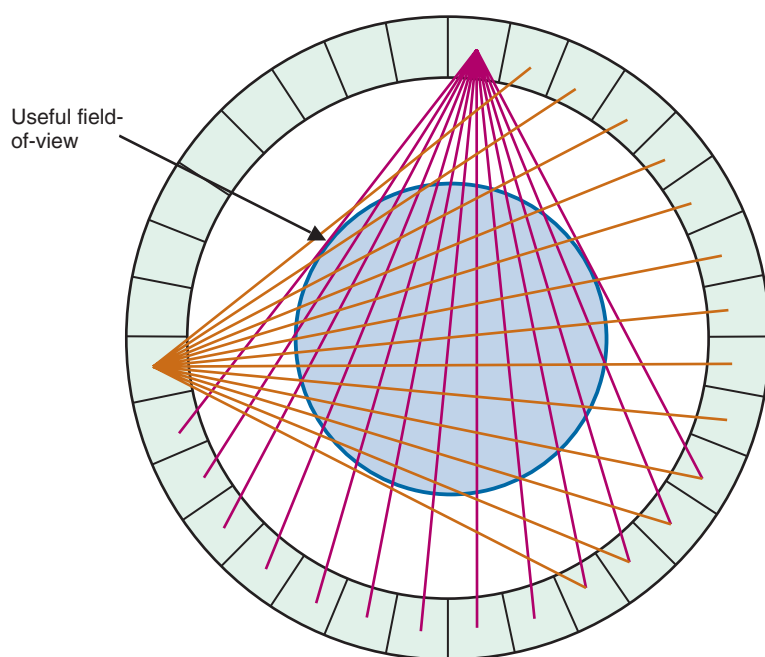


**FIGURE 18-12** Ring of detectors in which individual elements are operated in coincidence with multiple elements on the opposite side of the ring. In multicoincidence operation, each detector element is associated with a fan-beam acquisition, shown for two individual detector elements in the drawing. Data are recorded simultaneously for all possible fan beams. The inner circle formed by edges of all such fan beams defines the useful field-of-view.



is moved axially toward the ends of the ring, the geometric efficiency still has a triangular shape. Thus the *average* geometric efficiency for a source distributed within the sensitive volume for ACD across the width of the ring is half the value given by Equation 18-8, that is,

$$\bar{g}_{ACD,RING} \approx \frac{h}{2D} \quad (18-9)$$

Equations 18-8 and 18-9 also are valid for polygonal arrays, with  $D$  representing the diameter of a circle drawn tangential to the surface of the array. As long as  $h \ll D$ , they also apply to continuous detectors that use gamma camera electronics, rather than discrete detector elements, to determine event locations.

In addition to increasing geometric efficiency and improving its uniformity, multicoincidence detection with a ring or polygonal array of detectors also allows simultaneous acquisition of multiple projection views without moving the detectors. Suppose the ring consists of  $N$  individual detector elements. When each detector in the ring or array is operated in coincidence with a bank of detectors on the opposite side, as illustrated in Figure 18-12, a total of  $N/2$  fan-beam projections are acquired. These fan-beam projections typically are arranged to form parallel-beam profiles, as illustrated in Figures 16-20 and 18-2. However, as illustrated in Figure 18-11, data from adjacent pairs of detector usually are assigned to the same projection profile, thereby decreasing the number of views to  $N/4$ .

The number of detectors that are enabled for multicoincidence detection determines the width of the fan-beam projections and thus the diameter of the useful FOV. Sources located within the circle illustrated in Figure 18-12 are seen in all projections. Once a source is included within the useful FOV, a further increase in fan-beam width does not increase the counts recorded from that source. Sources outside the circle are not seen in some views, which could be a cause of image artifacts (see Chapter 16, Section C.2). Typical PET systems operate with each detector in coincidence with approximately two-thirds the total number of detectors in the ring.

Geometric efficiency varies somewhat across the useful FOV of the detector ring. In part, this is because the solid-angle for coincidence detection changes with source position. There also are geometric effects caused by differences in angle of incidence of the

photons onto the detectors and by gaps between detector elements. Corrections for this and other image nonuniformities are described in Section D.1.

It is noteworthy that, by segmenting large detectors into smaller elements and operating them in coincidence with multiple elements in the opposing array, it is possible to improve the spatial resolution in PET with only a modest loss of geometric efficiency. This effect is seen in Equation 18-9, in which geometric efficiency depends on the diameter of the ring,  $D$ , but not on the width  $d$  of the individual detector elements. Most of the loss of sensitivity that does occur is due to the requirement for interelement spacing and shielding, which is only approximately 0.2 to 0.3 mm in practical systems. For comparison, from fundamental principles, the geometric efficiency of absorptive collimators is degraded approximately as the square of spatial resolution (Equation 14-8). This presents a formidable challenge for improving spatial resolution in imaging applications based on single-photon counting, including SPECT.

The benefits of multicoincidence operation extend as well to the third (axial) dimension in multi-ring PET systems. This is discussed further in Section C.

As is the case for any imaging system, the sensitivity of a PET system also depends critically on the detection efficiency of the detector, which enters as a squared term in Equation 18-6. As was discussed in Chapter 11, Section A.3, detection efficiency is given by

$$\varepsilon = 1 - e^{-\mu_l x} \quad (18-10)$$

where  $\mu_l$  is the linear attenuation coefficient of the detector material and  $x$  is the detector thickness. Values of  $\mu_l$  for several detector materials of interest for PET are given in Table 18-2. Also indicated are values of  $\varepsilon$  for 2-cm-thick detectors of each material, without a low-energy threshold and with an energy threshold that eliminates 50% of the detected pulses. Values for  $\varepsilon^2$  in this table are useful for calculating scanner sensitivity and ACD counting rates (Equation 18-6). These values illustrate why materials such as BGO, LSO, and LYSO (Chapter 7, Section C.4) are preferred over NaI(Tl) for PET imaging.

Overall sensitivities for PET systems for a small-volume source of activity located near the center of the scanner range from 0.2% to 0.5% (0.002-0.005 cps/Bq) for single-ring systems or for multi-ring systems operated in

TABLE 18-2  
LINEAR ATTENUATION COEFFICIENTS AND DETECTION EFFICIENCIES FOR SOME  
SCINTILLATORS AT 511 keV\*

Scintillator	$\mu_{\text{p}}(511 \text{ keV}) \text{ cm}^{-1}$	$\varepsilon \text{ (2 cm)}^\dagger$	$\varepsilon^2 \text{ (2 cm)}$	$\varepsilon_{50} \text{ (2 cm)}^\ddagger$	$\varepsilon_{50}^2 \text{ (2 cm)}$
NaI(Tl)	0.34	0.49	0.24	0.25	0.061
BGO	0.95	0.85	0.72	0.43	0.18
LSO, LYSO	0.88	0.83	0.69	0.41	0.17
GSO	0.70	0.75	0.57	0.38	0.14
BaF <sub>2</sub>	0.44	0.58	0.34	0.29	0.086

\*Efficiency values are for 2-cm thick crystals.  
†Detection efficiency (see Equation 18-10), assuming no low-energy threshold (all pulses counted).  
‡Detection efficiency, assuming low-energy threshold is used, with 50% of pulses counted ( $f = 0.5$  in Equation 11-4).

2-D acquisition mode (one slice per ring; Section C.1). For multi-ring systems in which coincidences between rings are allowed for 3-D data acquisition (see Section C.2), the sensitivity typically is 2% to 10% (0.02-0.10 cps/Bq). For comparison, the sensitivities for SPECT systems with a general-purpose parallel-hole collimator are in the range of 0.01% to 0.03% (0.0001-0.0003 cps/Bq), depending on the number of detector heads (see Chapter 14, Section E.7). The substantially greater sensitivity of PET versus SPECT systems is due primarily to their ability to achieve a high degree of spatial resolution without the use of absorptive collimators.

9. Event Types in Annihilation Coincidence Detection

ACD produces an output whenever two events are recorded within a specified coincidence timing window. Generically, any such

events are called *prompt coincidences*. The discussion and analysis presented thus far assumes that all prompt coincidences arise from a pair of photons produced from the same annihilation event and that the annihilation event occurs somewhere within the coincidence volume between the detectors (see Fig. 18-1). These events are called *true coincidences*. Equation 18-6 describes the sensitivity of the system for these events. However, other prompt coincidence events also can occur within the resolving time of the detector system.

Two examples are shown in Figure 18-13. *Random coincidences* (also called *accidental coincidences*) occur when annihilation photons from two unrelated positron annihilation events are detected in two different detectors, within the coincidence timing window, and recorded as a single coincidence event. This can happen if one photon from each annihilation event is detected in each detector element.

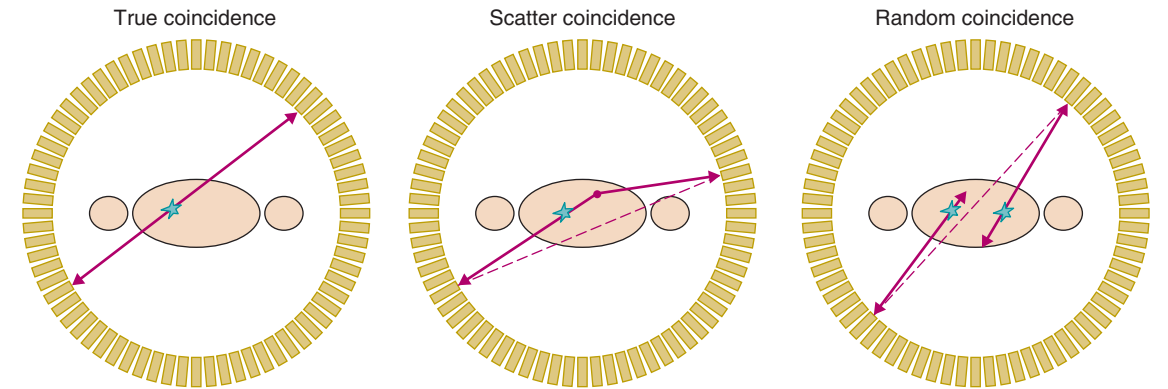


FIGURE 18-13 True coincidence event (left), scatter coincidence event (center), and random or accidental coincidence (right). Scatter and accidental coincidences yield incorrect positional information and contribute a relatively uniform background to the image that results in a loss of contrast. (Courtesy Dr. Magnus Dahlbom, University of California—Los Angeles.)

Random coincidences are not rare events, because the volume of tissue from which the photons for a random coincidence event could arise generally is much larger than the potential volume for true coincidence events.

The random coincidence counting rate in a detector pair is given by

$$R_{\text{random}} = \Delta T \times R_{\text{single},1} \times R_{\text{single},2} \quad (18-11)$$

where  $\Delta T$  is the coincidence timing window used by the system\* and  $R_{\text{single},1}$  and  $R_{\text{single},2}$  are the single-channel counting rates in the two detectors of the pair. Unlike true coincidence events, which can occur only when the source is located within the volume that is geometrically defined by the sides of the detector pair (see Fig. 18-1), random coincidences can arise from activity anywhere in the region between the detectors, including activity outside the useful FOV for a ring or array of detectors. Thus the single and random coincidence counting rates depend in a complicated way on both the source and detector geometry. A detailed analysis of these factors is beyond the scope of this text. Reference 1 provides a more comprehensive analysis. Nonetheless, some general observations can be made.

In general, the greater the total amount of activity used in a study, the higher the ratio of random-to-true coincidence rates. This is because the random coincidence rate increases as the square of the amount of activity present (product of single-channel counting rates in Equation 18-11), whereas the true coincidence rate increases only linearly with the amount of activity administered (Equation 18-6). A second general observation is that the ratio of random-to-true coincidence rates decreases in proportion to the width of the coincidence timing window. However, as noted in Sections A.1 and A.2, there are lower limits for this value, because of electronic and time-of-flight considerations. Finally, a general way to reduce the single-channel counting rate from activity outside the true coincidence volume is to use tungsten septa to restrict the FOV of individual detectors (see Section B.3). In turn, this reduces the random coincidence rate.

In actual PET scanners, the ratio of random-to-true coincidence counting rates typically ranges from approximately 0.1 to 0.2 for brain imaging to greater than 1 for applications where large amounts of activity may be nearby, but outside the true coincidence volume of the scanner. The latter could apply, for example, to some types of abdominal imaging when large amounts of activity are excreted into the bladder. Random coincidences occur more or less uniformly across the FOV of the scanner, causing a loss of image contrast as well as inaccuracies in quantification of activity within the patient. Methods for correcting for random coincidences are discussed in Section D.2.

A second category of nonvalid prompt coincidences are *scatter coincidences*. These occur when one (or both) of the photons from an annihilation event outside the sensitive volume for true coincidence events undergoes scattering and is detected in a detector other than the one that would be appropriate for a true coincidence event. The scattering event shown in Figure 18-13 occurs within the patient, but it also can occur within components of the scanner. Because the two annihilation photons were emitted simultaneously, they reach the detectors virtually simultaneously, apart from small time-of-flight differences (see Section A.2). Because these differences are very small, the detector system and its associated coincidence logic cannot typically distinguish them from valid events.

As is the case for the random-to-true coincidence ratio, the ratio of scatter-to-true coincidence counting rates depends in a complicated way on the source distribution and detector geometry. Placement of lead shielding on either side of the detector ring, or of thin tungsten septa between detector rings in a multi-ring PET system, reduces the likelihood of accepting scattered photons. However, unlike the random-to-true ratio, the scatter-to-true ratio does not depend on the amount of activity administered, because both the scatter and true coincidence rates increase linearly with this parameter. It also does not depend on the width of the coincidence timing window because scatter coincidences arise from the same positron annihilation event, and the two photons actually do arrive almost simultaneously at the two detectors. In clinical studies, the scatter-to-true coincidence ratio ranges from 0.2 to 0.5 for brain imaging and from 0.4 to 2 for abdominal imaging. The higher end of these ranges applies for 3-D

\*The value of  $\Delta T$  used here refers to the time separation between any two events that is determined by the electronics to indicate a prompt coincidence event (see Chapter 8, Section F). This differs from the definitions used in some articles and texts and leads to an additional factor of 2 in the version of Equation 18-11 in those publications.

acquisitions, which do not use interplane septa (see [Section C.2](#)).

Scatter coincidences provide incorrect localization of the positron annihilation event. The degree of position error depends on the scattering angle and location of the scatter event. Scatter coincidences lead to a broad distribution of mispositioned events, generally peaked toward the center of the object. Methods for minimizing the acceptance of scattered photons and for correcting for residual scatter coincidences are discussed in [Section D.3](#).

## B. PET DETECTOR AND SCANNER DESIGNS

As discussed in [Section A.6](#), detection efficiency ([Equation 18-10](#)) is an important parameter in PET scanner sensitivity and performance. Sodium iodide detectors, which are the “workhorse” for many nuclear medicine applications, also have been used for PET scanners. Indeed, as discussed in [Section B.3](#), it is possible to use appropriately modified dual-headed SPECT systems for PET imaging. However, because of the relatively high energy of the 511-keV annihilation photons, sodium iodide generally is not the detector material of choice for PET imaging. For these reasons, most PET scanners use denser higher-Z scintillation detectors arranged in rings or banks of discrete elements around the scanned object. These systems not only provide a high detection efficiency but they allow the simultaneous collection of data for all projection angles with a completely stationary set of detectors. In this section, we discuss the design of modern PET detector systems and scanners. Reference 2 is a useful review describing emerging detector technologies for PET.

### 1. Block Detectors

Early PET systems used individual detector units consisting of a piece of scintillator coupled to a photomultiplier tube (PMT). The individual detectors were arranged in a ring or in multiple rings around the subject. As illustrated in [Figure 18-4](#), the response profile at midplane of a pair of coincidence detectors is a triangle with FWHM equal to one half the width of the detector. Thus to improve the intrinsic resolution of a PET scanner, the detectors must be made smaller. However, the cost increases rapidly if each detector element requires its own PMT.

The *block detector*, designed in the mid-1980s by Casey and Nutt,<sup>3</sup> allows small detector elements to be used (improving spatial resolution) while reducing the number of PMTs required to read them out (controlling cost). [Figure 18-14](#) shows a typical block detector. A large piece of scintillator (most commonly BGO, LSO, or LYSO), is segmented into an array of many elements by making partial cuts through the crystal with a fine saw. The cuts between the elements are filled with a reflective material that serves to reduce and control optical cross-talk between scintillator elements. The array of crystals is read out by four individual PMTs. The depth of the saw cuts is determined empirically to control the light distribution to the four PMTs in a fairly linear fashion.

To determine the segment of the crystal in which an annihilation photon is detected, the signals from a four-PMT array are combined as follows:

$$X = \frac{(PMT_A + PMT_B) - (PMT_C + PMT_D)}{PMT_A + PMT_B + PMT_C + PMT_D}$$

$$Y = \frac{(PMT_A + PMT_C) - (PMT_B + PMT_D)}{PMT_A + PMT_B + PMT_C + PMT_D}$$
(18-12)

where  $PMT_A$ ,  $PMT_B$ , and so forth are the signals from different PMTs. It will be recognized that these are essentially identical to [Equations 13-1 and 13-2](#) for position localization for an Anger camera, except that only four PMTs are used here. The  $X$  and  $Y$  signals then are used to determine the subelement of the array in which the annihilation photon was detected.

[Figure 18-15](#) shows the image obtained from uniform irradiation of a block detector. The image is not uniform. Rather, the calculated locations for recorded events are clustered in small localized areas corresponding to the individual detector elements. There is a small amount of overlap, but the individual elements are clearly resolved. Although the array pattern is nonlinear, the separation is sufficiently clear to allow each (x,y) location in the image to be assigned to a specific detector element in the array, for example, by using a look-up table.

The major advantage of the block detector is that it enables many detector elements (e.g.,  $8 \times 8 = 64$ ) to be decoded using only four PMTs. This dramatically lowers the cost per detector element while providing high spatial



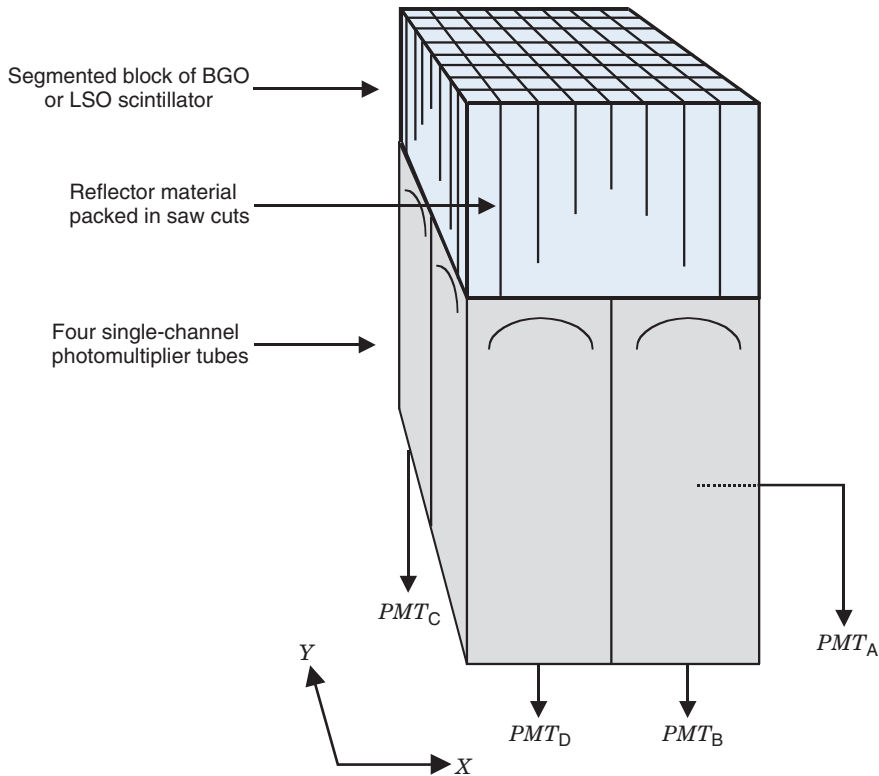


**FIGURE 18-14** Block detector commonly used in clinical PET scanners. A piece of BGO or LSO scintillator is cut into an array of smaller elements that are read out using four single-channel photomultiplier tubes (PMTs). The cuts in the material are filled with an opaque reflective material that, along with the depths of the cuts, helps control the distribution of scintillation light reaching the PMTs.

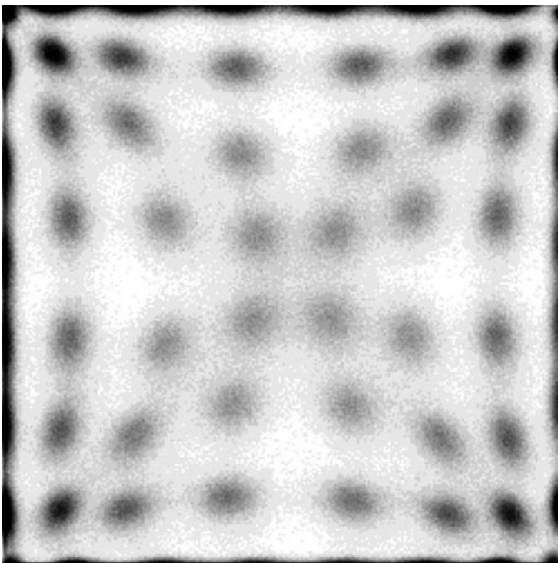


**FIGURE 18-15** Flood-field image obtained by uniformly irradiating a block detector with 511-keV annihilation photons. Individual block detector elements appear as distinct “blobs” in the image, allowing separation of events recorded within individual detector elements.

resolution. Typical block detectors are made from 20- to 30-mm-thick BGO, LSO, or LYSO scintillator crystals (see Chapter 7, Section C.4), with 4- to 6-mm-wide sub-elements.

## 2. Modified Block Detectors

Two important modifications have been made to the basic design of the block detector. The first is to use proportionately larger PMTs positioned so they overlap portions of adjacent blocks (Fig. 18-16). Thus each block still is monitored by four PMTs, but each PMT also monitors the corners of four different blocks. This approach, known as *quadrant sharing*, reduces the total number of PMTs required for the array by approximately a factor of four as compared with the basic block design described in the preceding section. (The actual reduction is slightly smaller, as a result of edge effects.)

Quadrant sharing is used to create large planar detector panels that can be combined in hexagonal or other polygonal arrangements in a PET system. These detector panels closely resemble a standard gamma camera detector

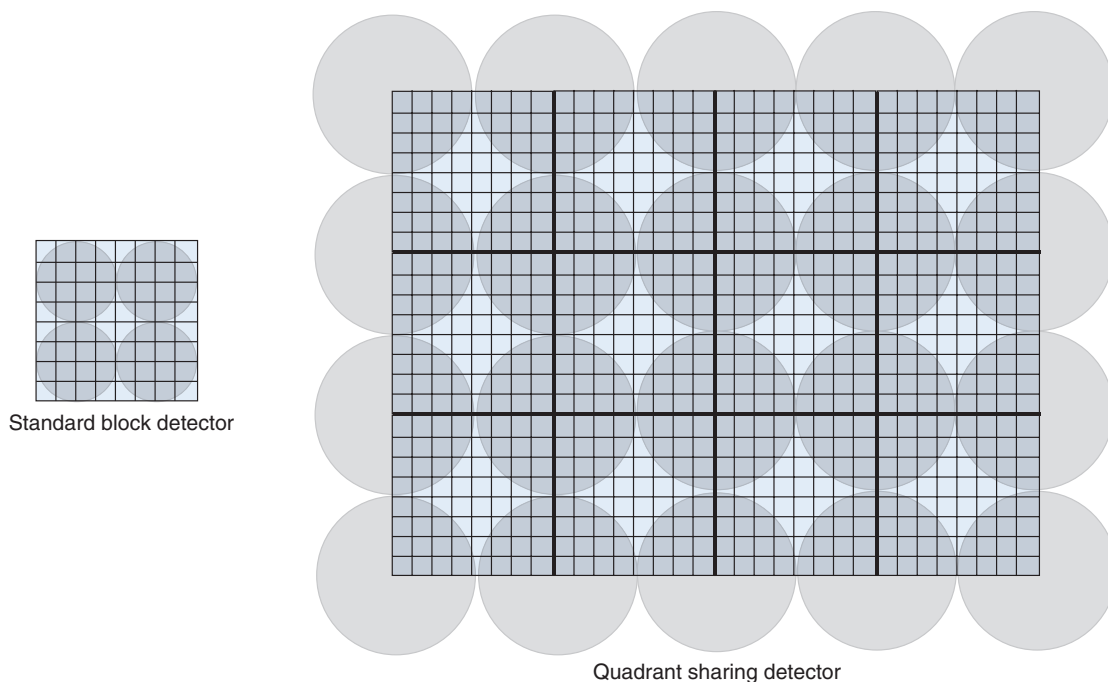


**FIGURE 18-16** *Right*, Quadrant-sharing detector, in which each scintillator block straddles the corners of four photo-multiplier tubes (PMTs). This allows larger PMTs to be used as compared to a standard block detector (*left*). For large panels, this leads to almost a fourfold reduction in the number of PMTs required to read out a given number of scintillator elements.

(Chapter 13, Section B), with the continuous scintillator plate replaced by an array of discrete scintillator elements. Although this approach reduces the cost per detector element of a PET system (by reducing the number of PMTs and electronic channels required compared with a block detector), it has the disadvantage of higher dead time losses, because each PMT views signals from a larger volume of scintillator.

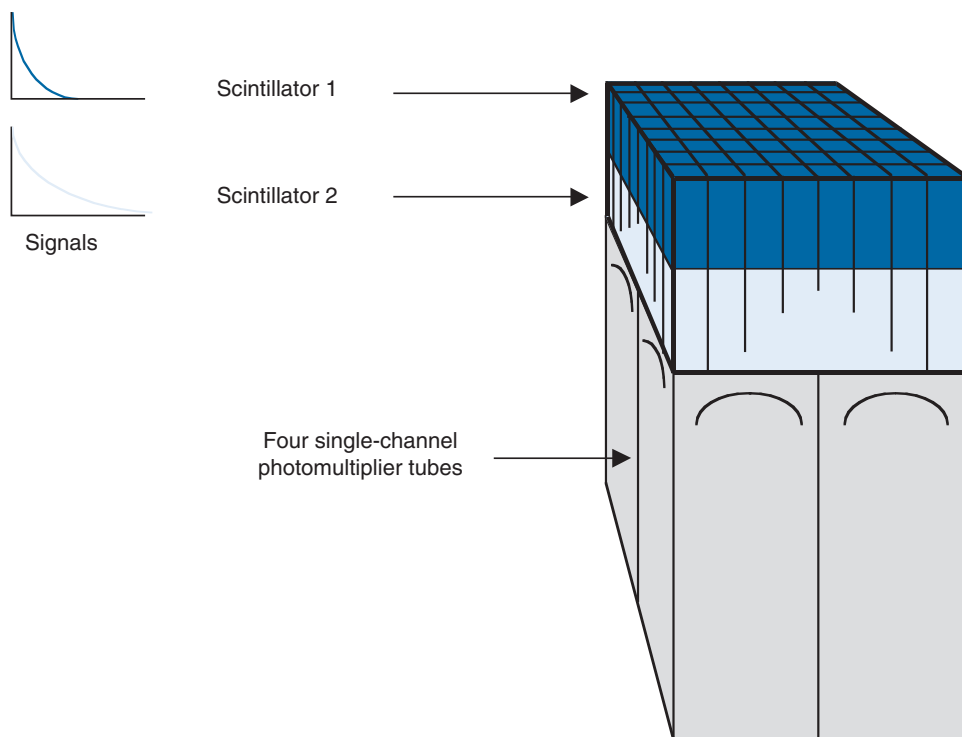
The second modification of the basic block detector design is to use layers of two different scintillator materials, creating what is known as a *phoswich* (Fig. 18-17). This approach makes use of the difference in decay times of the two scintillators. By monitoring the decay time of the pulse, the event can be localized into either the upper or lower layer. For example, combinations of LSO (decay time  $\sim 40$  nsec) and GSO (decay time  $\sim 60$  nsec) scintillators can be used. Because the location of photon interaction can be determined to within half the total scintillator thickness, this reduces the DOI effects (described in Section A.5) by approximately a factor of 2. The disadvantage of this approach is that manufacturing of the detectors is more involved and that the light output and stopping power of GSO are worse than LSO. Thus

the overall detector performance is slightly degraded as compared with a detector of the same dimensions made purely from LSO. The phoswich design also can be combined with the quadrant-sharing approach.

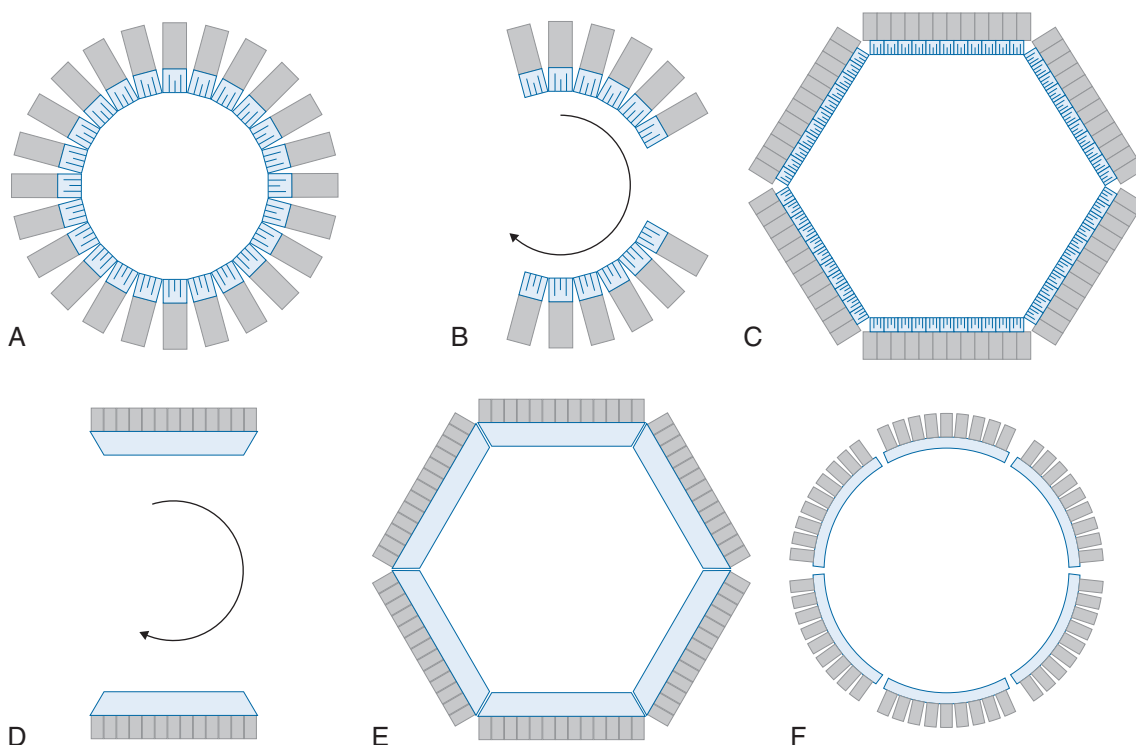
### 3. Whole-Body PET Systems

Figure 18-18 illustrates several different whole-body PET scanner designs that have been developed, some using block detectors comprising discrete scintillator elements as introduced previously (*A*, *B*, *C*) and others that use continuous large-area gamma camera detectors (*D*, *E*, *F*). Systems that use a stationary ring or polygonal array of detectors (*A*, *C*, *E*, and *F*), with the detectors operating in multicoincidence mode, can acquire data for all projection angles simultaneously and these designs have been the basis for most commercial systems. Others (*B*, *D*) use only a few opposing banks of detectors, which must be rotated to get full tomographic information. Most PET systems use a ring diameter of 80 to 90 cm. After inserting scatter shielding and a shroud to cover the detectors and other components, the clear bore of the scanner typically is 55 to 60 cm, which is sufficient to comfortably accommodate most patients. The FOV in the axial direction is determined by the axial





**FIGURE 18-17** Phoswich detector constructed from two scintillator materials with different decay times. By analyzing pulse decay time, an event can be assigned to either the upper or lower layer, reducing the effective thickness of the detector by one half and providing some depth of interaction information.



**FIGURE 18-18** PET scanner geometries based on discrete scintillator elements (*top row*) or continuous scintillator plates (*bottom row*). *A*, Full ring of modular block detectors. *B*, Partial ring of modular block detectors. *C*, Hexagonal array of quadrant-sharing panel detectors. *D*, Dual-headed gamma camera with coincidence circuitry. *E*, Hexagonal array of gamma camera detectors. *F*, Continuous detectors using curved plates of NaI(Tl). A complete set of profiles can be acquired without motion with systems shown in *A*, *C*, *E*, and *F*, whereas detector motion is required with systems shown in *B* and *D*.

extent of the detectors and typically is in the range of 15 to 40 cm.

Figure 18-19 shows schematically the design of a representative whole-body PET scanner based on block detectors. This scanner employs 336 BGO block detectors, arranged in three rings of 112 blocks per ring.<sup>4</sup> Each block is cut into a  $6 \times 6$  array of elements, with element sizes of 4 mm (transaxial)  $\times$  8.1 mm (axial)  $\times$  30 mm

(thickness). The inside diameter of the detector ring is 92.7 cm and the clear bore of the scanner is 59 cm. The 18 crystals (three rings of three blocks) in the axial direction cover an axial FOV of 15.2 cm. The gantry can be tilted  $\pm 20$  degrees from the vertical, which can be useful for aligning the scan planes with the optimal viewing angle for an organ of interest. The system contains a set of tungsten interplane

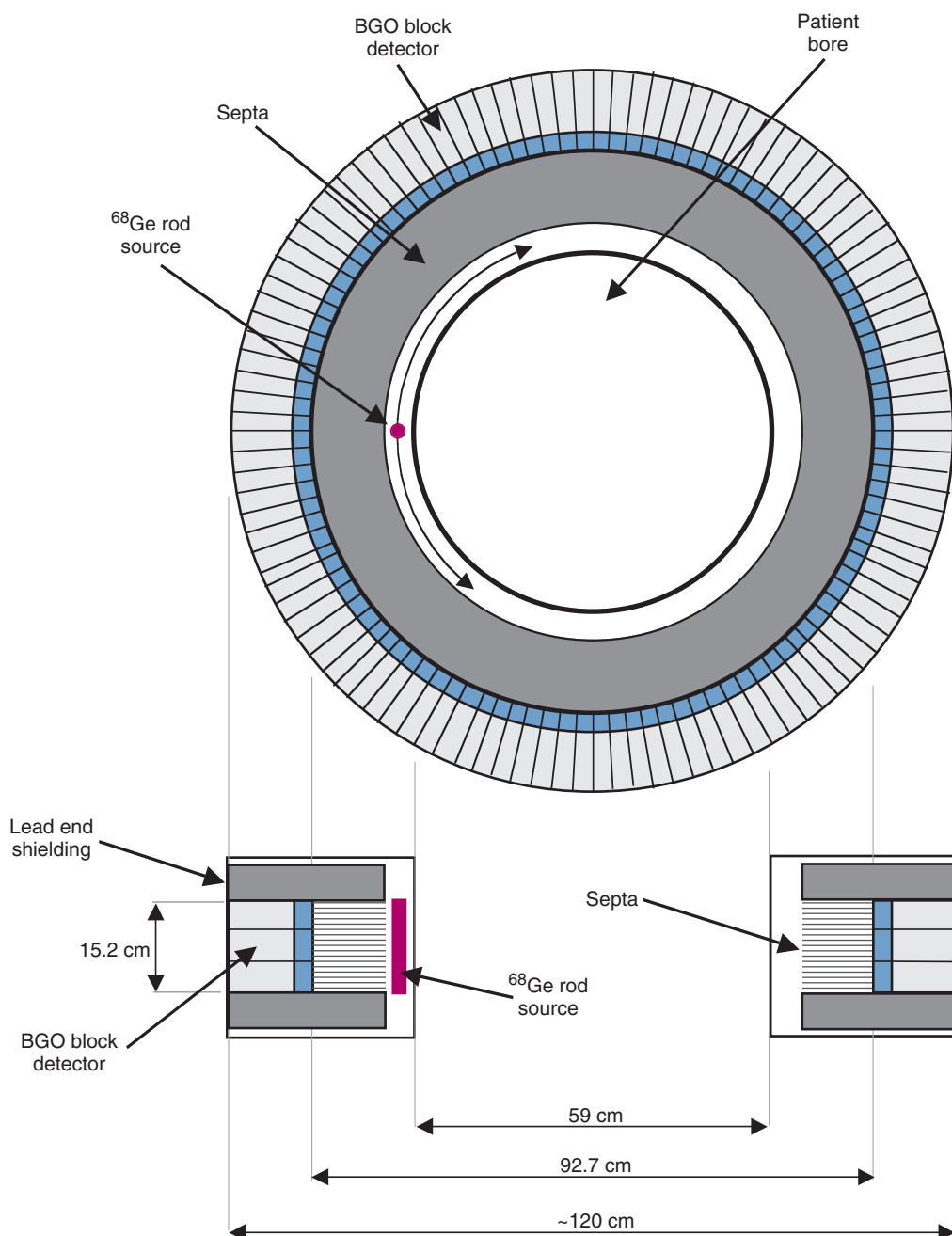


**FIGURE 18-19** Drawings showing transaxial (*top*) and axial (*bottom*) cross-sections through a representative whole-body PET scanner.

septa of 1-mm thickness and 12-cm length between the crystal rings. The septa can be extended or retracted to provide varying levels of scatter rejection, as described in more detail in [Section C.2](#). They also provide shielding from potential high concentrations of activity outside the scanning volume of interest, which helps control the random and scatter coincidence rates, as described in [Section A.9](#).

The scanner also incorporates a rod source made from  $^{68}\text{Ge}$  ( $T_{1/2} = 273$  days) to perform transmission scans for attenuation corrections. The source is permanently mounted in the system and is retracted into a lead shield when not in use. This is discussed further in [Section D.4](#). Typically, the system uses a coincidence timing window of 12.5 nanoseconds and an energy window of 300 to 650 keV. The intrinsic spatial resolution of the detectors is approximately 3 mm, whereas the system resolution is approximately 4.5 mm near the center of the FOV and approximately 6.2 mm near the periphery of the scanner bore, the difference being due primarily to DOI effects (see [Section A.5](#)). The axial (slice thickness) resolution is approximately 4.2 mm at the center of the scanner, whereas near the periphery of the FOV, approximately 20-cm distance axially from the center, it is approximately 6.9 mm. The scanner simultaneously acquires data for 35 slices, separated center-to-center by 4.25 mm, in 2-D acquisition mode. In 3-D acquisition mode (see [Section C.2](#)), the number of slices and slice thickness in the axial direction can be chosen arbitrarily.

[Figure 18-20](#) shows photographs for another whole-body PET scanner, which is described in reference 5. This system has smaller detector dimensions in the axial

direction and uses the scintillator LYSO. Its design and performance capabilities are broadly similar to those of the scanner described previously. The trend in recent years has been to improve spatial resolution by further reducing the dimensions of the detector elements (4 mm  $\times$  4 mm is current state-of-the-art), and to increase the number of detectors along the axial direction to improve axial coverage of the body, increase sensitivity and thus reduce imaging times for studies that cover the whole body. A second trend has been to improve the detectors and electronics to provide sufficient timing resolution that time-of-flight information (see [Section A.2](#)) can be extracted. Commercial systems with a coincidence timing resolution of better than 600 psecs (corresponding to a spatial localization of  $\sim 9$  cm) are now available.

Gamma camera technology similar to that used for conventional planar imaging and SPECT (see Chapters 13, 14, and 17) also has been employed for PET imaging. In one approach, coincidence timing circuitry has been installed between the heads of dual-headed scanners and the collimators removed for PET imaging. The spatial localization provided by the detector heads allows many coincidence lines to be acquired simultaneously. The basic concept is illustrated in [Figure 18-18D](#). These systems can still be used for planar or SPECT imaging, by replacing the collimators.

The performance of standard gamma cameras for PET suffers from a number of limitations. Chief among these is the relatively low detection efficiency of the camera detectors for 511-keV annihilation photons (see Figs. 11-4 and 11-5). As well, although removing the collimator allows simultaneous

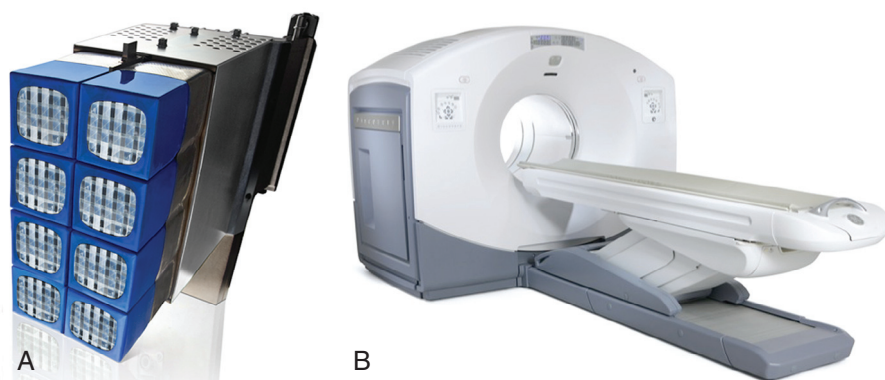


**FIGURE 18-20** A, Modular cassette from a PET scanner containing eight block detectors. These cassettes are mounted on the PET scanner gantry to form complete rings of detector blocks that surround the patient. B, Clinical PET scanner based on rings of these block detectors. (Courtesy GE Healthcare, Waukesha, WI.)

data acquisition for many projection angles, the resulting high counting rates can lead to significant dead time losses and pile-up effects. An event detected anywhere in the detector can affect all other events detected at the same time. By contrast, dedicated PET systems use blocks of detectors that operate essentially independently from each other. Random and scatter coincidence rates, both of which increase with the geometric efficiency for detecting events outside the true-coincidence volume (see Section A.9), also tend to be high when the collimators are removed from the camera heads.

Some manufacturers addressed these limitations by incorporating thicker NaI(Tl) crystals (up to 2.5 cm) into systems intended for PET usage, and by employing more sophisticated circuitry in their gamma cameras to minimize dead time and suppress pile-up effects (see Chapter 14, Section A.4). Other manufacturers have developed gamma camera detectors specifically for use in PET. One such scanner used six curved gamma camera detector plates, arranged in a ring around the object (Fig. 18-18F). At the present time, PET scanners based on continuous gamma camera detectors are not widely used.

PET systems have been integrated with x-ray computed tomography (CT) technology to create combined PET/CT scanners in a single gantry. Almost all PET scanners sold today are combined with CT. These multi-modality systems are discussed in Chapter 19.

#### 4. Specialized PET Scanners

Specialized PET systems also have been developed for high-resolution brain imaging and for breast imaging. These systems have smaller-diameter detector rings or arrays for improved geometric efficiency. They also generally have smaller detector elements for higher spatial resolution. Figure 18-21 shows a scanner designed for brain imaging that incorporates 2.1-mm  $\times$  2.1-mm dimension scintillator elements in a phoswich configuration (Fig. 18-17) to limit DOI degradation of spatial resolution.<sup>6</sup> The detectors are based on the quadrant sharing design (Fig. 18-16) and eight detector panels are arranged in an octagonal configuration around the head. The reconstructed spatial resolution of images from this system is  $\sim$ 2.5 mm, superior to the 4- to 6-mm resolution that can be obtained on whole-body PET systems. Blurring caused by nonlinearity is reduced, as the detector separation in this brain imaging system is only 47 cm.

Figure 18-22 shows an example of a PET system developed for breast imaging.<sup>7</sup> This system uses two scanning detector panels (area 16.4 cm  $\times$  6 cm) to image the breast under mild compression. With scanning motion, the FOV can be adjusted up to 16.4 cm  $\times$  24 cm. The system uses LYSO scintillator elements with dimensions of 2 mm  $\times$  2 mm  $\times$  13 mm and these are read out using position-sensitive PMTs. Not all projection angles are measured, as the detectors do not rotate about the breast. However, as all points on one

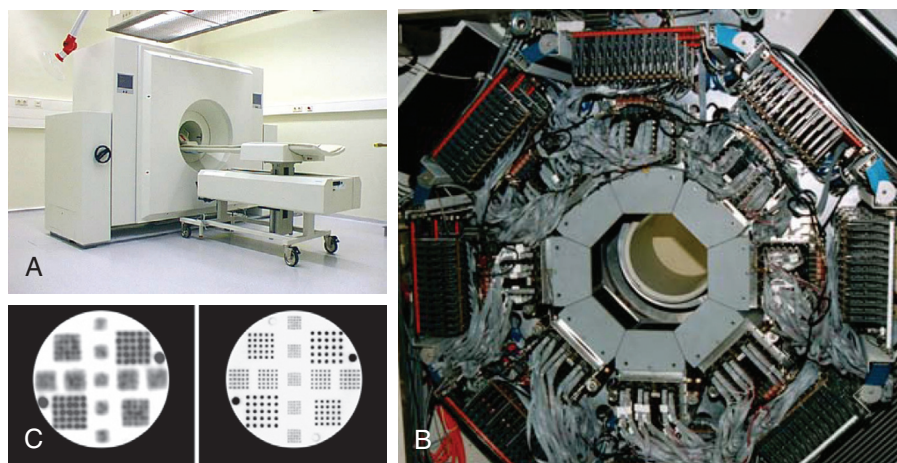


**FIGURE 18-21** A, Photograph of a high-resolution brain imaging system. B, Interior of the scanner, showing the eight panels of detectors arranged in an octagonal geometry that are made up of phoswich detectors read out by photomultiplier tubes in a quadrant-sharing configuration. C, Phantom images from this system (right) compared with those obtained from a typical whole-body PET scanner (left). The improvement in spatial resolution arising from the smaller detector dimensions is apparent. (Courtesy Dr. Adriaan Lammertsma VU Medical Center, Amsterdam, Netherlands, and Siemens Medical Solutions, Knoxville, TN.)





**FIGURE 18-22** A PET system designed for breast imaging. Two detector panels scan back and forth to acquire an image of the breast under mild compression. (Courtesy Naviscan Inc., San Diego, CA.)

detector are in coincidence with all points on the opposing detector, there is sufficient angular information for approximate tomographic reconstruction using iterative reconstruction algorithms. The spatial resolution achievable with such systems is on the order of 2 to 2.5 mm for image planes parallel to the detector plates. In addition to improving geometric efficiency, the cost of dedicated breast PET systems is lower compared with whole-body scanners, because the volume of detector material is much smaller. Attenuation effects also are reduced, as the annihilation photons only need traverse the breast tissue, and not the entire cross-section of the body, for detection.

### 5. Small-Animal PET Scanners

PET scanners that are designed for small-animal imaging studies also are available. These are typically being used to evaluate and optimize new diagnostic and therapeutic agents destined for human use. The challenge is to obtain sufficiently high spatial resolution and sensitivity for imaging in mice and rats. Unlike SPECT imaging of small animals with pinhole collimators (Chapter 17, Section A.4), PET cannot readily improve the image resolution through magnification techniques, and

also has additional constraints because of positron physics and the DOI effects discussed in Sections A.4 and A.5. Fortunately, for small diameter systems, the blurring caused by noncolinearity (see Section A.4) is significantly reduced compared with whole-body clinical scanners. For a scanner with a 15-cm detector separation, this blurring is only 0.33 mm.

Most small-animal PET scanners use small scintillator elements decoded with position-sensitive or multichannel PMTs. The dimensions of the scintillator elements are typically on the order of 1 to 2 mm to achieve high spatial resolution. To avoid major DOI blurring, most systems only use a thickness of 10 to 15 mm of scintillator, and keep the ring diameter quite large (12 to 20 cm) compared with the size of the subject. Despite this, good sensitivity can be obtained, as high geometric efficiency can be achieved with relatively small amounts of detector material and the FOV required to cover the animal is quite small.

A typical small-animal PET scanner based on such technology is shown in Figure 18-23. The detector in this system consists of a block of LSO scintillator segmented into 1.5-mm ×



**FIGURE 18-23** A PET scanner designed specifically for small-animal imaging. Such systems can achieve a spatial resolution on the order of 1.5 mm. (Courtesy Siemens Preclinical Solutions, Knoxville, TN.)

1.5-mm  $\times$  10-mm elements in a  $20 \times 20$  matrix, and read out by a position-sensitive PMT, which has six anodes in the X-direction and six anodes in the Y-direction. The scanner uses 64 of these detector blocks arranged in four rings of 16 detector blocks per ring. The transaxial FOV of the system is 10 cm and the axial FOV is 12.7 cm. The system operates exclusively in 3-D acquisition mode (see Section C.2). The reconstructed spatial resolution of this system is approximately 1.4 mm, and the sensitivity is 7.4% for an energy window of 250-750 keV.<sup>8</sup>

Some small-animal PET systems incorporate alternative detector technologies. Successful devices have been constructed based on avalanche photodiode detectors (Chapter 7, Section C.3), multiwire proportional chamber detectors with high-density converters to improve the efficiency of these detectors for 511-keV photons (Chapter 7, Section A.3), or direct detection using the semiconductor cadmium zinc telluride (Chapter 7, Section B). A review of selected small-animal PET technology is presented in references 9 and 10.

## C. DATA ACQUISITION FOR PET

### 1. Two-Dimensional Data Acquisition

Originally, most PET scanners were designed with axial collimators or septa between each ring of detectors (see Fig. 18-19). As shown in Figure 18-24A, the septa allow only those photons that are emitted parallel to the plane of the detector ring to be detected. This is known as *2-D data acquisition*. The septa provide efficient rejection of annihilation photons that have been scattered in the body. They also reduce the single-channel counting rate, thereby lowering the random coincidence rate (Equation 18-11) and minimizing dead time losses.

Because each crystal ring collects data from a single slice (oblique lines of response are not allowed because of the septa), 2-D projection data are analogous to the data obtained with a rotating gamma camera with a parallel-hole collimator used for SPECT imaging. Thus the images can be reconstructed using filtered backprojection (Chapter 16, Section B) or iterative approaches (Chapter 16, Section D). Using a scanner that employs multiple detector rings, one obtains a series of contiguous 2-D transaxial image planes that can be stacked together to form an image volume.

With slight or no modification of the lengths of the septa, PET scanners also can acquire data from immediately adjacent rings, as shown in Figure 18-24, B. These are known as *cross planes*. At the center of the scanner, the cross planes fall exactly halfway between the direct planes that are defined by individual crystal rings. For purposes of analysis, the cross-plane data can be assumed to have been acquired with a virtual ring of detectors shifted by half the detector width along the axial direction relative to the direct planes. For a scanner with  $n$  detector rings, this leads to a total of  $(2n - 1)$  image planes in the axial direction. Because the cross planes receive data from two different lines of response, they have roughly twice the sensitivity (and therefore twice the counting rates) as the direct planes. They also are “x-shaped,” but the amount of this distortion is too small to have a practical effect, except at the periphery of the FOV, where it leads to additional blurring in the axial direction.

Cross-plane data are reconstructed in the same manner as direct-plane data. In PET scanners with very small detector elements, the number of cross planes can be increased even further to include crystal ring differences of  $\pm 2$ ,  $\pm 3$ , and so forth (Fig. 18-24C). As larger ring differences are accepted, the sensitivity increases; however, there is a loss of spatial resolution in the axial direction, because of the superposition of data that come from axially disparate locations.

### 2. Three-Dimensional Data Acquisition

Multi-slice 2-D data acquisition as described earlier rejects any photons that have an obliquity of more than the maximum accepted ring difference (typically  $\pm 2$  or 3 rings). This is very wasteful because the annihilation photons from many potentially valid coincidence events are absorbed by the septa. In *3-D acquisition mode*, the interplane septa are removed from the PET scanner and data are obtained for all possible lines of response, as shown in Figure 18-24D. Typically, this leads to a fourfold to eightfold improvement in sensitivity; however, the number of scattered photons and the single-channel counting rates also are increased. In brain scans using 3-D acquisition mode, 30% to 40% of the detected photons will have been scattered in the head prior to reaching the detectors. The axial sensitivity profile for 3-D acquisition is determined geometrically and is a triangular function, peaked at the center of the FOV. In 3-D mode, it is important to place the



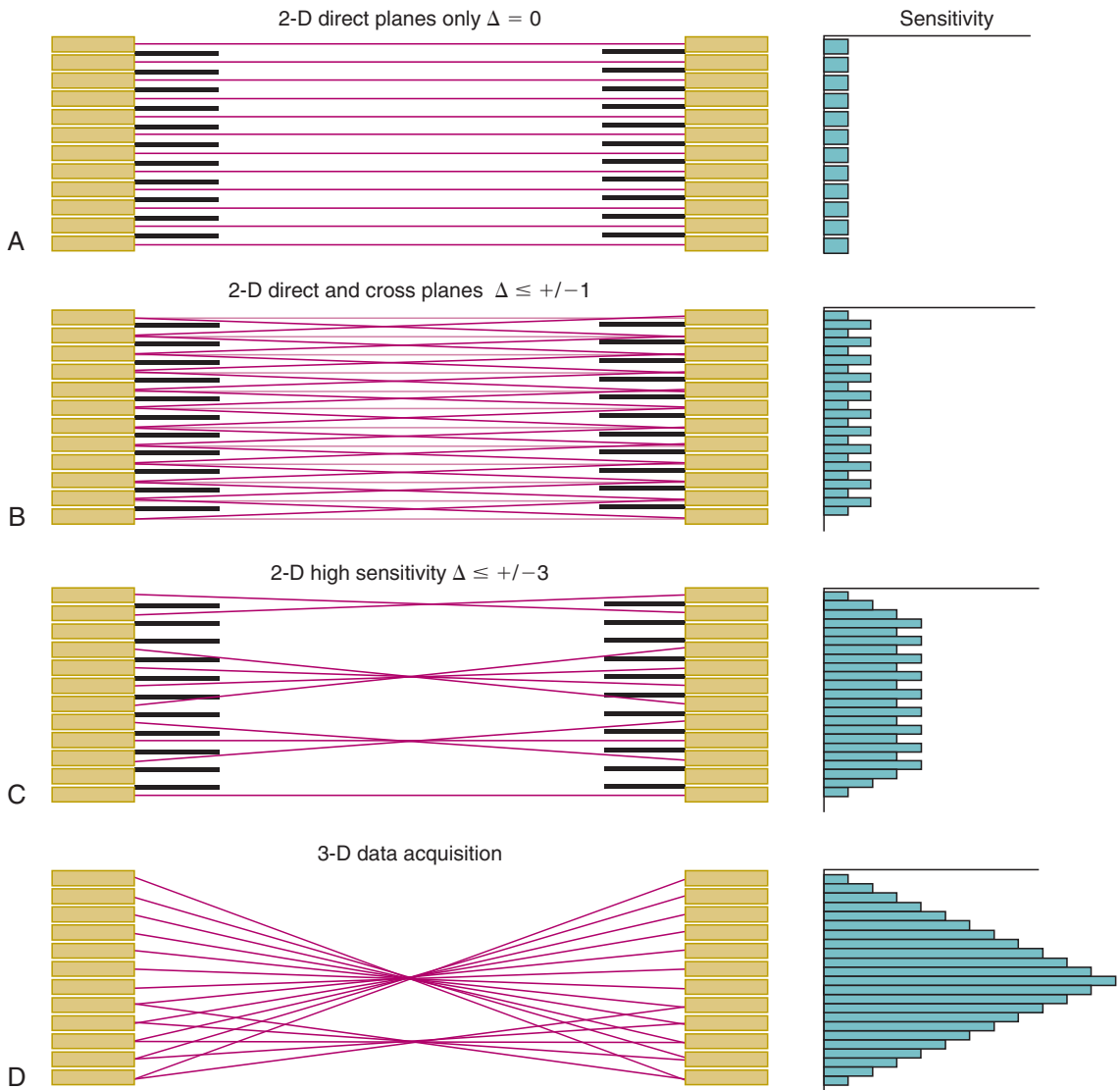


**FIGURE 18-24** Two-dimensional (2-D) and 3-D data acquisition schemes for PET. Axial cross-sections through a multi-ring scanner are shown on the *left* and corresponding axial sensitivity profiles on the *right*. *A*, 2-D direct plane data acquisition. *B*, 2-D direct and cross-plane data acquisition. *C*, 2-D high-sensitivity data acquisition. *D*, Full 3-D data acquisition. For clarity, lines of response are shown only for selected axial positions in *C* and *D*.

structures of interest as close to the center of the axial FOV as possible. Multi-ring PET systems have relatively high overall sensitivity, as shown by the following example.

### EXAMPLE 18-2

Consider a 32-ring PET scanner with BGO detector elements that are 6-mm-wide  $\times$  6-mm axial height  $\times$  2-cm-thick. The crystals are tightly packed on a 73.3-cm-diameter ring, such that each ring contains 384 crystals. In single-slice mode, each ring is operated in coincidence only with other detector elements within the same ring. In 3-D acquisition mode, each ring is operated in coincidence with all other rings. Estimate the sensitivity for a source located at the center of scanner bore for single-slice and 3-D modes. Assume that the source is comparable in size to the axial length of the detector crystals, and that a low-energy threshold that passes 50% of detected events is used.

#### Answer

For a small-volume source, comparable in size to the axial thickness of a single detector ring, Equation 18-9 applies. For such a source, the average geometric efficiency at the center of a single-ring is

$$\bar{g}_{RING} \approx \frac{1}{2} \times \frac{6 \text{ mm}}{733 \text{ mm}} \approx 0.00409 = 0.409\%$$

From Table 18-2, the intrinsic efficiency (squared) for coincidence detection with 2-cm-thick BGO crystals and an energy threshold that passes 50% of detected pulses is 0.18. When combined with geometric efficiency (Equation 18-6), this gives a total detection efficiency (sensitivity) for single-slice acquisition of

$$\begin{aligned} \text{Sensitivity}_{RING} &\approx 0.18 \times 0.00409 \\ &\approx 0.00074 = 0.074\% \end{aligned}$$

In 3-D mode, all 32 rings are operated in coincidence with each other (Fig. 18-24D). Because of the increased solid-angle of coverage, this immediately increases the geometric efficiency for a source located at the center of the axial FOV by approximately a factor of 32 (ignoring small geometric effects). As well, a small-volume source at the center of the axial FOV more closely approximates a true point source, for which Equation 18-8 applies. As

compared with Equation 18-9, this adds another factor of 2 to the sensitivity at the center of the FOV. The final result is

$$\begin{aligned} \text{Sensitivity}_{3D} &\approx 32 \times 2 \times 0.18 \times 0.00409 \\ &\approx 0.047 = 4.7\% \end{aligned}$$

For an extended source, for example, a line source that has length comparable to the total thickness of the 32-ring array, the average sensitivity of the scanner across the axial FOV is given by Equation 18-9, and the 3-D result given previously would be reduced by a factor of 2.

The estimated sensitivity in Example 18-2 for 3-D operation is 2-3 orders of magnitude greater than the sensitivity achieved with a gamma camera for single-photon imaging with absorptive collimation (see Chapter 14, Section E.7). Note as well that the additional rings extend the volume of coverage, so that a volume of tissue can be imaged in less time with a multi-ring scanner, as compared with a single-ring device.

Reconstruction of 3-D PET data also is more complex, because the projection data arises not only from transverse slices used for 2-D reconstruction, but also from many oblique angles through the subject. Thus the full 3-D image volume must be considered during the reconstruction process. Fully 3-D Fourier-based and iterative reconstruction algorithms are both available; however, computation times are roughly an order of magnitude longer than for 2-D reconstructions, because they involve backprojections and computations in three dimensions rather than two. Approximate 3-D reconstruction algorithms have been developed in which the 3-D dataset is reduced to a 2-D dataset using rebinning methods (see Chapter 16, Section E.3). In many situations, any loss in accuracy resulting from the approximations made in these algorithms is small when compared with the benefit of enabling 3-D PET data to be reconstructed in clinically acceptable timeframes.

Despite the increased computational and data storage requirements for 3-D PET, the large increases in sensitivity that it produces has resulted in it being offered as an option on all commercial whole-body PET systems. In some systems, interplane septa have been completely eliminated and only 3-D acquisition is possible. All small-animal and breast

imaging systems currently operate in 3-D mode. Reference 11 provides further details on 3-D data acquisition and reconstruction in PET.

### 3. Data Acquisition for Dynamic Studies and Whole-Body Scans

PET scanners having detectors that surround the patient can acquire profiles simultaneously for all of the projection angles required for reconstruction. This allows dynamic studies to be performed with frame times of just a few seconds. For a dynamic scan, the number of time frames required and the length of each frame typically are entered into the computer. The scan starts as the tracer is being injected and the location to which the data are sent in the computer memory is incremented at the end of each frame.

Some systems allow what is called *list-mode acquisition*. In this mode, each coincidence event is written sequentially to a computer disk, along with a time stamp that indicates when the event occurred. After the scan is completed, the result is a single file with a list of coincidence events in the order that they were received. The events in this list can then be integrated over any time interval, allowing the number and duration of frames to be chosen and altered as necessary, after a scan has been completed. For example, this may allow the elimination of segments of data where a patient moved.

Once the projection data have been organized into frames, each corresponding to a certain time interval, the frames are individually reconstructed into tomographic images using the methods described in Chapter 16. In many studies, the dynamics of tracer delivery, accumulation, and clearance are important indicators of tissue function. The data often are analyzed using mathematical models described in Chapter 21.

Whole-body studies are performed by translating the patient through the scanner and acquiring data at multiple axial locations. This is achieved by using a computer-controlled bed. In 3-D PET, to improve the uniformity in sensitivity along the axial direction, bed positions are typically overlapped by 1/4 or 1/3 of the axial FOV. The data from different bed positions then are “stitched” together to form a single whole-body image.

## D. DATA CORRECTIONS AND QUANTITATIVE ASPECTS OF PET

One goal of tomographic imaging is that the intensity of the reconstructed image should be proportional to the amount or concentration of activity at the corresponding location in the object. This is desirable for accurate comparisons of activity levels in different organs or in diseased versus normal tissues. It is essential for some types of dynamic studies (see Chapter 21). A number of corrections are required to achieve this goal in SPECT, as described in Chapter 17, Section B. In this section, we describe similar corrections that are needed in PET.

### 1. Normalization

PET scanners that are based on gamma camera detectors require corrections for non-linearity and nonuniformity similar to those that are employed in SPECT (see Chapter 17, Section C.4). Inaccurate correction of these factors can lead to rings or other artifacts in reconstructed images.

A typical PET scanner may have 10,000 to 20,000 individual detector elements, which may have small variations in dimensions or in the fraction of scintillation light that is coupled to the PMTs. There also may be differences in the effective thickness of crystal seen by photons traveling along different angles of incidence for different cross planes. Correction for these variations is known as *normalization*.

Conceptually, the most straightforward approach to normalization would be to record the number of counts detected by each coincidence detector pair while exposing all pairs to the same radiation source. This could be accomplished, for example, using a rod source that extends through the axial FOV and rotating it around the periphery of the FOV (see Fig. 18-19). (This could be the same source that is used for attenuation correction, described in Section D.4.) One revolution of the rod source around the FOV would expose all detector pairs to the same number of annihilation photon pairs.

In an ideal scanner, each detector pair ( $i, j$ ) would record the same number of counts  $N$  (within statistical limits) in the rod source scan. In practice, some detector pairs record more counts and some record less counts because of efficiency variations. The

normalization factor for a specific pair of detectors is computed from

$$Norm_{i,j} = \frac{N_{i,j}}{\langle N \rangle} \quad (18-13)$$

where  $\langle N \rangle$  is the average value of  $N(i,j)$  for all of the coincidence detector pairs in the scanner. Hence, the average normalization factor is equal to 1.

The normalization factor then is used to correct the counts recorded for each detector pair in a scan of a patient,  $C(i,j)$ , as follows:

$$C_{Norm_{i,j}} = \frac{C_{i,j}}{Norm_{i,j}} \quad (18-14)$$

where  $C_{Norm_{i,j}}$  are the corrected counts. This correction is applied to the projection (sinogram) data prior to image reconstruction.

Statistical errors caused by the finite number of counts in the normalization scan will increase the noise levels in the corrected data, which is undesirable. In 3-D mode, PET scanners can have on the order of  $10^8$  lines of response. To achieve a statistical uncertainty of  $\sim 3\%$  in the normalization factor would therefore require a normalization scan with a total of approximately  $1000 \times 10^8 = 10^{11}$  counts. Even at relatively high total counting rates of approximately 500,000 cps, this would require approximately 55 hours of scanning time. Thus the straightforward approach outlined previously must be modified to reduce the number of counts required without increasing statistical noise. Most of the modified methods are based on computing the efficiencies of the individual detector elements (rather than all possible detector pairs) and then combining them to estimate the efficiency of the detector pairs. Details of these methods are beyond the scope of this text but are discussed in reference 12.

## 2. Correction for Random Coincidences

As discussed in Section A.9, random coincidences add a relatively uniform background across the reconstructed image, suppressing contrast and distorting the relationship between image intensity and the actual amount of activity in the image. There are two approaches to estimating the random coincidences so that they can be subtracted from the measured projection data: the *delayed window* method and the *singles* method.

In most PET scanners, the arrival time of each photon is recorded and “tagged” with an accuracy of approximately 2 nanoseconds. At

the end of each clock cycle (typically 256 nanoseconds), the computer checks to see if any events have occurred, and if so, whether they occurred with arrival times within  $\Delta T$  nanoseconds of each other, where  $\Delta T$  is width of the coincidence timing window (typically 4 to 12 nanoseconds). If two photons arrive within this time interval, they are recorded as a valid event and the appropriate memory location corresponding to that particular detector pair is incremented by +1.

An estimate of the random coincidence rate can be obtained by delaying the coincidence timing window by a time that is much greater than its width. For example, the coincidence timing window might be delayed by 64 nanoseconds, for example, from 64 to 76 nanoseconds for a 12-nanosecond window. With this amount of time delay, only events that have arrival times separated by between 64 and 76 nanoseconds are accepted. No true (or scattered) prompt coincidences will be detected in the delayed window, because photons from the same decay will always arrive at the detectors within a few nanoseconds of each other. However, the rate of random coincidences will be the same in the delayed and undelayed windows because the rate at which uncorrelated photons strike the detector is the same for both windows. Thus the delayed window count provides an estimate of the number of random coincidence events. This number is subtracted from the total number of coincidence events for the detector pair. The correction occurs on-line in most PET systems and usually is transparent to the user.

The events recorded in the delayed window are not the same ones as are recorded in the undelayed window. Rather, the delayed window provides a separate and independent measure of the random event rate. Subtracting the number of random events recorded in the delayed window results in an increase in the statistical noise level for the measurement (see Chapter 9, Section C.1). Specifically, if  $N_{true}$  is the number of true coincidence events recorded,  $N_{scatter}$  the number of scatter coincidences, and  $N_{random}$  is the number of random coincidences subtracted from the total, the uncertainty in the remaining (true plus scatter) coincidences is

$$\sigma(N_{true} + N_{scatter}) = \sqrt{(N_{true} + N_{scatter}) + (2 \times N_{random})} \quad (18-15)$$

Thus even if accurate corrections can be made, the random coincidence rate should be

minimized to avoid unduly increasing the statistical noise level of the image.

The second method for estimation of random coincidences is based on [Equation 18-11](#). If the rate at which single (not coincidence) events occur in each detector is measured, and the coincidence timing window  $\Delta T$  is known, then the rate of random coincidences for any pair of detectors can be computed. Because the rate of single events is typically at least an order of magnitude higher than the rate of coincidence events, the statistical noise level in the estimate of the number of random events is small in comparison with that in the measurement of the number of prompt coincidences, and the uncertainty in the remaining coincidences after random coincidences have been subtracted is given by

$$\sigma(N_{\text{true}} + N_{\text{scatter}}) \approx \sqrt{N_{\text{true}} + N_{\text{scatter}} + N_{\text{random}}} \quad (18-16)$$

This method requires that each detector module continuously monitors the rate at which it is detecting single events.

### 3. Correction for Scattered Radiation

Scattered radiation in PET imaging leads to a hazy background in the reconstructed images, generally more concentrated toward the center of the image. As with random coincidences, this leads to a decrease in image contrast and to errors in the quantitative relationship between image intensity and the amount of activity in the object. The fraction of scattered events in PET can be very high, especially in 3-D imaging of the abdomen, where it may be as high as 60% to 70%. This large value has three major causes. First, only one of the two annihilation photons needs to be scattered for a scatter coincidence to occur. Second, the energy resolution of PET detectors using dense scintillators such as BGO and LSO is inferior to NaI(Tl) detectors because of their lower light output. This requires the use of a wider pulse-height analyzer window to capture the photopeak events. Finally, the predominant mode of interaction in scintillators at 511 keV is Compton scattering, and many unscattered annihilation photons deposit less than 511 keV of energy in the detector. Thus to increase the detection efficiency for photons that undergo Compton scattering in the crystal, the analyzer window is widened even further to capture these events.

It is not possible to distinguish between scatter events in the body versus scatter events in the detector crystal on the basis of pulse amplitude. Therefore simple correction schemes based on dual-energy windows are far less successful in PET imaging than in SPECT imaging. Two main approaches currently are used for scatter correction in PET. The first approach uses information from the original scatter-contaminated image and transmission image (see [Section D.4](#)) to derive the correction. The emission image shows the distribution of the activity in the subject. The transmission image reflects the attenuation coefficient of the tissue. At 511 keV, virtually all attenuation is due to Compton scatter. Using these two images and computer modeling of photon interaction physics (see Chapter 6, Section C.3) with some simplifying assumptions, it is possible to derive an estimate of the underlying distribution of scattered events and their contribution to individual profiles. The estimated contribution of scattered radiation then is subtracted from the projection profiles and the reconstruction is repeated with the scatter-corrected data.

As described in Chapter 19, Section E, with the advent of hybrid PET/CT scanners, the scatter distribution also can be computed from the registered CT images, in which the CT image is used in place of a PET transmission image. This method works very well when all the sources of radioactivity that could lead to detected scatter events are contained within the FOV of the scanner. When large amounts of activity are just outside the FOV of the scanner, problems can arise. Another drawback of this approach is that it is computationally intensive.

A second method for scatter correction is based on an examination of projection profiles immediately outside the object. After correcting for random coincidences, the only events that should fall into these projection elements are those that are mispositioned because of scatter. Based on the premise that scatter is a low-frequency phenomenon with little structure, data from the tails of the projection profiles can be extrapolated using simple smoothly varying functions across the entire projection. Both gaussian and cosine functions have been used for this purpose. The extrapolated scatter distribution then is subtracted from the projections prior to image reconstruction. This method is rapid and, because it involves a direct measurement of scatter levels, it accounts for scatter from radioactivity outside the FOV. However, it can



only approximate the true scatter distribution and, in situations in which the scatter distribution is complex, or when the object fills the whole FOV with no portion of the profile to examine outside the object, the technique may result in significant errors. These can range from a few percent for brain imaging to tens of percent at the heart-lung interface.

#### 4. Attenuation Correction

Attenuation correction is by far the largest single correction in PET. Fortunately, the correction is relatively easy to derive. Consider a source located at a depth  $x$  inside an object of thickness  $T$  as shown in Figure 18-25. Both of the photons from an annihilation event in the source must be detected to record a valid event. Assuming that they are emitted in the appropriate directions, the probability that both photons will reach the detector is given by the product of their individual probabilities

$$P_{\text{det}} = e^{-\mu x} \times e^{-\mu(T-x)} = e^{-\mu T} \quad (18-17)$$

where  $\mu$  is the linear attenuation coefficient of tissue at 511 keV and is approximately  $0.095 \text{ cm}^{-1}$  for soft tissue,  $0.12$  to  $0.14 \text{ cm}^{-1}$  for bone, and  $0.03$  to  $0.04 \text{ cm}^{-1}$  for lung. Note that the probability that both photons will reach the detector is independent of the source location along the line joining the two detectors.

Equation 18-17 is similar to Equation 17-5 for the geometric mean in SPECT, except that it applies for all source distributions, whereas the geometric mean equation applies only for point or plane sources at a fixed depth,  $x$ . As was the case for SPECT, transmission measurements can be used to correct for attenuation in PET. In PET, two measurements are taken with a source located on a line joining each pair of coincidence detectors. The first

measurement, called the *blank scan*, is made without the subject in the scanner. The subject then is placed in the scanner and the measurement is repeated. This is known as the *transmission scan*. The attenuation correction factor  $A$  for a detector pair  $(i,j)$  is given by

$$A_{i,j} = \frac{\text{Blank}_{i,j}}{\text{Trans}_{i,j}} \quad (18-18)$$

where  $\text{Blank}_{i,j}$  and  $\text{Trans}_{i,j}$  are the counts in the blank and transmission scans for the detector pair.

To obtain transmission data for all coincidence detector pairs, it is necessary to scan the transmission source around the scanning volume for both the blank and transmission scans. Typically, a rod source, with its length extending along the axis of the scanner, is placed in a holder near the surface of the scanner bore, and the holder rotates around the central axis so that data are acquired for all pairs. The most commonly used source material is  $^{68}\text{Ge}$  (parent of  $^{68}\text{Ga}$ ,  $T_{1/2} = 273$  days). The blank scan needs to be performed only once a day because it remains constant over a period that is short compared with the half-life of the radionuclide in the rod source. The transmission scan is performed prior to injecting the patient with the radiotracer. It is important that the patient not move between the transmission and emission scan. Otherwise serious artifacts can occur, including the appearance of areas of abnormally high or low radiotracer uptake.

Conceptually, the simplest approach is to obtain the transmission scan before injecting the radiotracer to be imaged. This eliminates any possible interference between the activity that is present for the two scans.

A second approach, called *postinjection transmission scanning*, is to perform the

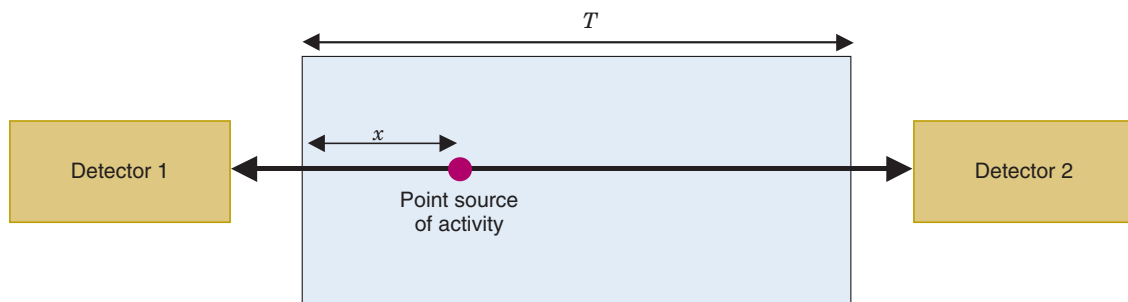


FIGURE 18-25 Parameters involved in the derivation of attenuation correction for PET (equation 18-17 in the text).



transmission scan immediately after the emission scan but while there is still radiotracer activity in the patient. This can save a significant amount of time, because the patient does not have to be on the table waiting for uptake after the transmission scan before the emission scan is performed. Another advantage of this approach is that it reduces the chances of patient motion and misalignment between the emission and transmission scans. However, it requires the ability to distinguish transmission events from emission events caused by residual radiotracer in the body. This is possible because the emission radiations generally are emitted from locations spread throughout the body, whereas the transmission radiations are emitted from a very small volume. Thus the transmission source irradiates only a small subset of detector pairs at any one time, and its counting rate in those irradiated pairs generally is much higher than the counting rate in the same detectors caused by emission radiations. To implement this method, the scanner must have the means to track the location of the transmission source and identify which detectors are being irradiated by it. A disadvantage of the postinjection approach is that the count-rate performance of the detectors must be sufficient to handle the emission and transmission activities simultaneously.

Finally, it is possible to acquire transmission and emission data at the same time. This approach, known as *simultaneous emission/transmission scanning*, is the most efficient way to use scanner time in many situations. As with postinjection transmission scanning, it is necessary to track the location of the rod source. Because the rod source irradiates only a small and known subset of detector pairs at any one time, emission data can be acquired simultaneously from the remaining nonirradiated pairs. For irradiated detector pairs, the counting rate from the transmission source is much higher than the emission counting rate, so the emission counts do not seriously affect the accuracy of the transmission data.

A disadvantage of simultaneous emission/transmission scanning is that the relatively “hot” transmission source can contribute random and scatter coincidence events to the emission data. Even with corrections, these events contribute to statistical noise and some degradation of image quality. For this reason, postinjection transmission scanning generally is the preferred approach.

Although these techniques work well, the widespread use of hybrid PET/CT scanners has significantly reduced the use of transmission scans using external radionuclide sources for attenuation correction. Instead, information from the CT scan is used to perform attenuation correction. The methods for CT-based attenuation correction are discussed in Chapter 19, Section E.

## 5. Dead Time Correction

Like all radiation detectors, PET detectors exhibit dead time and pile-up effects at high counting rates. The mispositioning of events caused by pile-up and possible approaches for minimizing pile-up described in the context of the gamma camera (see Chapter 14, Section A.4) apply as well to block detectors used for PET. Dead time corrections must be applied. Otherwise, the amount or concentration of radioactivity will be underestimated at high counting rates. Most PET scanners use empirical dead time models in which the observed counting rate as a function of radioactivity concentration is measured for a range of object sizes and at different energy thresholds. The resulting data are then fit with paralyzable or nonparalyzable dead time models (see Chapter 11, Section C.2). Some systems apply a global dead time correction factor for the system, whereas others apply corrections to individual pairs of detector modules.

Dead time losses are dominated by the single-channel counting rate, which are much higher than the coincidence counting rate. Corrections can be as large as a factor of 2, although generally it is desirable to keep them below this level. Situations in which the corrections can be large include first-pass cardiac studies, imaging studies near the bladder when there are high levels of excreted radioactivity, and studies with very short-lived radiotracers, such as  $^{15}\text{O}$ , which require high starting levels of activity to maintain adequate counting statistics over the course of a study.

## 6. Absolute Quantification of PET Images

All of the corrections described earlier are applied to the projection or sinogram data prior to reconstruction of the image. If accurately applied, after reconstruction, the voxel intensity in the image will be directly proportional to the amount of radioactivity in that voxel. Calibration to absolute concentrations of radioactivity usually is accomplished by

scanning a cylinder containing a uniform solution of a known concentration. The calibration factor CAL is defined as

$$\text{CAL} = \frac{\text{counts per pixel/radionuclide}}{\text{concentration in cylinder (kBq/cm}^3\text{)}} \quad (18-19)$$

The voxel intensity in the image of the subject is divided by the calibration factor to obtain calibrated images in kBq/cm<sup>3</sup>. To obtain the absolute amount of activity in the voxel (becquerels), one would have to multiply this result by the voxel volume.

Quantification in PET is subject to the same partial-volume effects as were discussed in Chapter 17, Section B.5, for SPECT imaging. This effect occurs for structures of size smaller than  $2 \times \text{FWHM}$  of the imaging system. Structures that have dimensions smaller than this will have their radioactivity concentrations either overestimated or underestimated depending on the regional distribution of the radioactivity. An example of where this becomes important is in the quantification of activity in thin layers of cerebral cortex.

## E. PERFORMANCE CHARACTERISTICS OF PET SYSTEMS

A set of standardized methodologies have been agreed upon for measuring important parameters that describe the performance of PET scanners. Published standards exist both for clinical whole-body scanners<sup>13</sup> and for small-animal scanners.<sup>14</sup> In a similar fashion to the tests described for SPECT systems (see Chapter 17, Section C), measurements of spatial resolution and sensitivity are based on carefully designed acquisition and reconstruction protocols that enable some degree of comparison of performance across different systems. Protocols for measuring the fraction of scattered and random coincidences, losses resulting from dead time, image quality, and quantitative accuracy of attenuation and scatter corrections also are prescribed. Full details can be found in references 13 and 14.

A commonly quoted performance parameter, incorporated in these standards, is the *noise equivalent counting rate* (NECR). This parameter, which is specific to PET systems, accounts for the additional statistical noise introduced by the correction for random and

scattered coincidences. The NECR is defined as the equivalent counting rate that gives rise to the same statistical noise level as the observed counting rate after random and scattered coincidences have been corrected for.

A PET scanner measures a prompt coincidence rate ( $R_{\text{prompt}}$ ) that comprises true coincidences ( $R_{\text{true}}$ ), scatter coincidences ( $R_{\text{scatter}}$ ) and random coincidences ( $R_{\text{random}}$ ). The rate of true coincidence events is given by

$$R_{\text{true}} = R_{\text{prompt}} - R_{\text{scatter}} - R_{\text{random}} \quad (18-20)$$

The NECR is defined as<sup>13</sup>

$$\text{NECR} = \frac{R_{\text{true}}^2}{R_{\text{true}} + aR_{\text{scatter}} + bR_{\text{random}}} \quad (18-21)$$

It usually is plotted as a function of activity, as both the rate of random coincidences and count losses caused by dead time are activity dependent. The constant  $a$  is the fraction of the projection that is occupied by the object being imaged. The constant  $b$  is equal to 1 if the singles method is used for randoms estimation and 2 if the delayed windows method is used (see Section D.2).

The prompt and random coincidence rates are measured. The rate of scattered coincidences is estimated by imaging a phantom that contains a line source. Events in the projection data that do not intersect the known location of the line source (after random coincidences already have been subtracted) must have been scattered.

It has been demonstrated that the NECR is roughly proportional to the square of the signal-to-noise ratio of the reconstructed activity values when the object is a cylinder with a uniform activity concentration.

Figure 18-26 shows typical NECR curves for a particular PET scanner and phantom. At higher activities, the NECR actually decreases because the rate of random coincidences increases as roughly the square of the activity, and dead time losses also reduce the observed counting rate. Often the peak NECR rate, and the activity concentration at which it is achieved, is reported. However, the values strongly depend on the size of the object that is imaged, and other factors such as the energy and timing windows, and the activity distribution within the phantom. Nonetheless, assuming the phantom used to acquire the NECR data is a reasonable approximation of the object that is to be imaged in a particular clinical or research task, the NECR

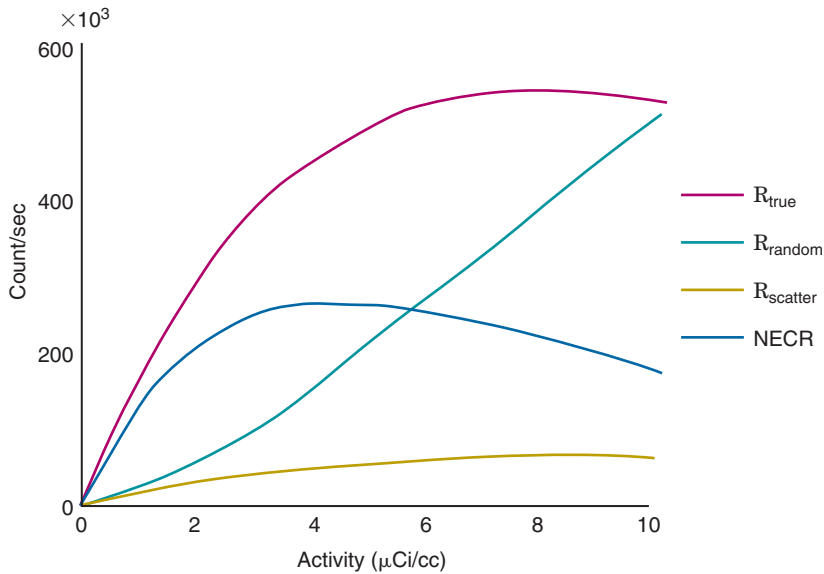


**FIGURE 18-26** Example of various coincidence counting rates and noise equivalent counting rate (NECR) for a clinical whole-body scanner. These data predict that for the phantom used in this study, the best signal-to-noise (corresponding to the peak of the NECR curve) in the reconstructed image would be achieved with an activity concentration of  $\sim 4 \mu\text{Ci/cc}$  ( $\sim 150 \text{ kBq/cc}$ ).

provides a useful guide for estimating the activity concentrations that provide the highest signal-to-noise ratio images. In some cases, it may not be possible to reach this activity concentration because of radiation dosimetry considerations (see Chapter 22). Measurements of NECR for a well-defined phantom can be useful for comparing the performance of different scanners, and estimations of NECR also can help guide the design and development of new PET scanners.

## F. CLINICAL AND RESEARCH APPLICATIONS OF PET

PET has major clinical applications in oncology, neurology, and cardiovascular disease.  $^{18}\text{F}$ -fluorodeoxyglucose (FDG) is by far the most commonly used radiotracer for clinical studies. The uptake of FDG reflects glucose metabolism in tissues. Many pathologic conditions can cause regionally specific alterations in glucose metabolism that can be detected using FDG-PET. PET's most widespread application has been for the detection and staging of cancer, for which whole-body FDG studies have become an important tool in staging patients and for deciding patient management. A whole-body FDG study is shown in Figure 18-27.

FDG also is used diagnostically in conjunction with blood flow tracers such as



**FIGURE 18-27** Whole-body  $^{18}\text{F}$ -fluorodeoxyglucose PET scan (injected activity 370 MBq) of a patient with cancer, showing widespread metastatic disease (dark spots). The scan took 14 minutes to acquire (7 overlapping bed positions to cover thorax and abdomen, 2 minutes per bed position), with imaging commencing 60 minutes post-injection. (Courtesy Dr. Paul Shreve, Spectrum Health, Grand Rapids, MI and Siemens, Medical Solutions USA, Inc., Knoxville, TN.)

$^{13}\text{N}$ -ammonia or  $^{82}\text{RbCl}$  to evaluate myocardial viability and stratify patients with coronary artery disease with regard to bypass surgery. In the brain, PET is used diagnostically in a range of neurodegenerative diseases (Alzheimer's disease, Parkinson's disease) and dementia, for epilepsy, neurodevelopmental disorders and in psychiatric disorders. Metabolic FDG images of a patient with Alzheimer's disease compared with those of a normal control are shown in Figure 18-28.

Many other PET radiotracers are used for research studies and are being developed for future clinical use. These include radioligands that bind to specific receptors systems in the brain, and radiotracers that target cell-surface molecules specific to certain types of tumors. Positron-emitting radionuclides also have been used to radiolabel cells (e.g., stem cells) and drug delivery vehicles such as nanoparticles. Many of these radiotracers are first evaluated in animal models using a dedicated animal PET scanner. Figure 18-29 shows an image of the binding of the radioligand  $^{11}\text{C}$ -raclopride to dopamine receptors in the rat brain.

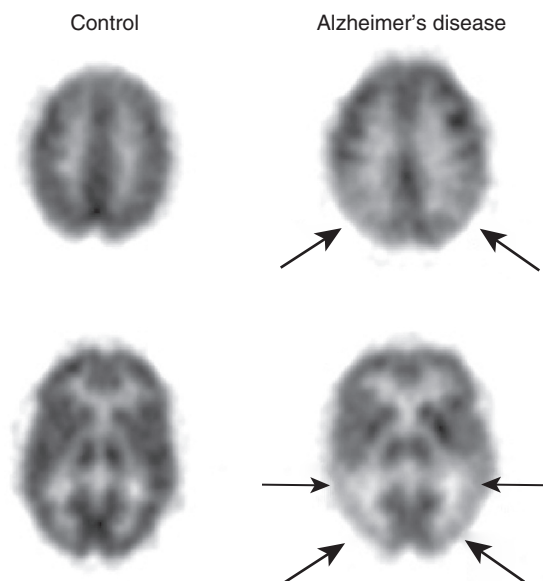


**FIGURE 18-28** Transaxial image slices showing  $^{18}\text{F}$ -fluorodeoxyglucose uptake at two different levels of the brain in a normal volunteer (control) and in a patient at an early stage of Alzheimer's disease. Data acquisition times were ~30 minutes and injected doses were 370 MBq (10 mCi). Arrows indicate metabolic deficits in the patient's images. This distinct pattern of reduced metabolism is seen in all patients with Alzheimer's disease and increases in severity and extent are seen as the disease progresses.

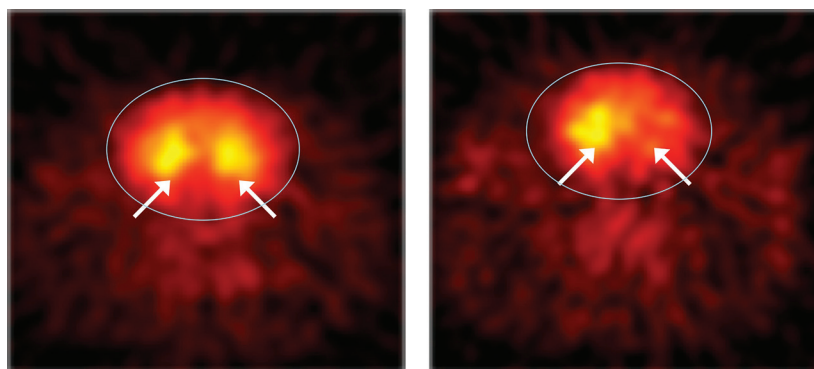


**FIGURE 18-29** Coronal image of rat brain acquired on a small-animal PET scanner following injection of  $^{11}\text{C}$ -raclopride. The location of the brain is indicated by the ellipse. This radiotracer binds to the dopamine receptors in the brain, which are located primarily in the striatum (arrows). Images were acquired before (left) and after (right) a pharmacologic intervention that damages the dopaminergic neurons on one side of the brain. A clear reduction in the binding of the radiotracer is observed on that side.

## REFERENCES

- Hoffman EJ, Phelps ME: Positron emission tomography: Principles and quantitation. In Phelps ME, Mazziotta JC, Schelbert HR, editors: *Positron Emission Tomography and Autoradiography: Principles and Applications for the Brain and Heart*, New York, 1986, Raven Press, pp 237-286.
- Lewellen TK: Recent developments in PET detector technology. *Phys Med Biol* 53:R287-317, 2008.
- Casey ME, Nutt R: A multicrystal two-dimensional BGO detector system for positron emission tomography. *IEEE Trans Nucl Sci* 33:460-463, 1986.
- Lewellen TK, Kohlmyer SG, Miyaoka RS, et al: Investigation of the performance of the General Electric ADVANCE positron emission tomograph in 3D mode. *IEEE Trans Nucl Sci* 43:2199-2206, 1996.
- Brambilla M, Secco C, Dominietto M, et al: Performance characteristics obtained for a new

- 3-dimensional lutetium oxyorthosilicate-based whole-body PET/CT scanner with the national electrical manufacturers association NU 2-2001 standard. *J Nucl Med* 46:2083-2091, 2005.
6. De Jong HWAM, van Velden FHP, Kloet RW, et al: Performance evaluation of the ECAT HRRT: an LSO-LYSO double layer high resolution, high sensitivity scanner. *Phys Med Biol* 52:1505-1524, 2007.
  7. MacDonald L, Edwards J, Lewellen T, et al: Clinical imaging characteristics of the positron emission mammography camera: PEM Flex Solo II. *J Nucl Med* 50:1666-1675, 2009.
  8. Constantinescu CC, Mukherjee J: Performance evaluation of an Inveon PET preclinical scanner. *Phys Med Biol* 54: 2885-2899, 2009.
  9. Rowland DJ, Cherry SR: Small-animal preclinical nuclear medicine instrumentation and methodology. *Sem Nucl Med* 38:209-222, 2008.
  10. Larobina M, Brunetti A, Salvatore M: Small animal PET: A review of commercially available systems. *Curr Med Imag Rev* 2:187-192, 2006.
  11. Bendriem B, Townsend DW: *The Theory and Practice of 3D PET*, Netherlands, Kluwer, 1998, Dordrecht.
  12. Badawi RD, Marsden PK: Developments in component-based normalization for 3D PET. *Phys Med Biol* 44: 571-594, 1999.
  13. Performance Measurements of Positron Emission Tomographs: *National Electrical Manufacturers Association (NEMA) Standards Publication NU2-2007*, Rosslyn, VA, 2007, NEMA.
  14. Performance Measurements of Small Animal Positron Emission Tomographs: *National Electrical Manufacturers Association (NEMA) Standards Publication NU4-2008*, Rosslyn, VA, 2007, NEMA.

## BIBLIOGRAPHY

**Additional general references are the texts indicated in references 1 and 11. Also pertinent are the following:**

- Phelps ME, editor: *Molecular Imaging and its Biological Applications*, New York, 2004, Springer-Verlag.
- Zanzonico P: Positron emission tomography: A review of basic principles, scanner design and performance, and current systems. *Sem Nucl Med* 34:87-111, 2004.